



**HAL**  
open science

# The surface-boundary layer connection across spatial scales of irrigation-driven thermal heterogeneity: An integrated data and modeling study of the LIAISE field campaign

Mary Rose Mangan, Oscar Hartogensis, Aaron Boone, Oliver Branch, Guylaine Canut, Joan Cuxart, Hugo de Boer, Michel Le Page, Daniel Martínez-Villagrasa, Josep Ramon Miró, et al.

## ► To cite this version:

Mary Rose Mangan, Oscar Hartogensis, Aaron Boone, Oliver Branch, Guylaine Canut, et al.. The surface-boundary layer connection across spatial scales of irrigation-driven thermal heterogeneity: An integrated data and modeling study of the LIAISE field campaign. *Agricultural and Forest Meteorology*, 2023, 335, pp.109452. 10.1016/j.agrformet.2023.109452 . hal-04274613

**HAL Id: hal-04274613**

**<https://hal.science/hal-04274613>**

Submitted on 8 Nov 2023

**HAL** is a multi-disciplinary open access archive for the deposit and dissemination of scientific research documents, whether they are published or not. The documents may come from teaching and research institutions in France or abroad, or from public or private research centers.

L'archive ouverte pluridisciplinaire **HAL**, est destinée au dépôt et à la diffusion de documents scientifiques de niveau recherche, publiés ou non, émanant des établissements d'enseignement et de recherche français ou étrangers, des laboratoires publics ou privés.



Distributed under a Creative Commons Attribution 4.0 International License

*Keywords*

## Highlights

**The surface-boundary layer connection across spatial scales of irrigation-driven thermal heterogeneity: An integrated data and modeling study of the LIAISE field campaign**

Mary Rose Mangan, Oscar Hartogensis, Aaron Boone, Oliver Branch, Guylaine Canut, Joan Cuxart, Hugo J. de Boer, Michel Le Page, Daniel Martínez-Villagrana, Josep Ramon Miró, Jeremy Price, Jordi Vilà-Guerau de Arellano

- Surface energy partitioning depends on the scale of the heterogeneity.
- The observed Bowen ratios range from 0.01-30, but the boundary layers were similar.
- The observed boundary layer is formed by surface fluxes at the regional scale.
- At local scales, non-local boundary-layer processes impact surface fluxes.

# The surface-boundary layer connection across spatial scales of irrigation-driven thermal heterogeneity: An integrated data and modeling study of the LIAISE field campaign

Mary Rose Mangan<sup>a,\*</sup>, Oscar Hartogensis<sup>a</sup>, Aaron Boone<sup>b</sup>, Oliver Branch<sup>c</sup>, Guylaine Canut<sup>d</sup>, Joan Cuxart<sup>e</sup>, Hugo J. de Boer<sup>f</sup>, Michel Le Page<sup>g</sup>, Daniel Martínez-Villagrasa<sup>e</sup>, Josep Ramon Miró<sup>h</sup>, Jeremy Price<sup>i</sup>, Jordi Vilà-Guerau de Arellano<sup>a</sup>

<sup>a</sup>*Meteorology and Air Quality Group, Wageningen University and Research, Wageningen, The Netherlands*

<sup>b</sup>*Météo-France/CNRS, Toulouse, France*

<sup>c</sup>*Institute of Physics and Meteorology, University of Hohenheim, Stuttgart, Germany*

<sup>d</sup>*Météo-France, Toulouse, France*

<sup>e</sup>*Department of Physics, University of the Balearic Islands, Palma, Spain*

<sup>f</sup>*Copernicus Institute of Sustainable Development, Environmental Sciences, Universiteit Utrecht, Utrecht, The Netherlands*

<sup>g</sup>*CESBIO, Centre d' Etudes Spatiales de la Biosphère, Univ. de Toulouse, CNRS, CNES, IRD, UPS, INRAE, Toulouse, France*

<sup>h</sup>*Meteorological Service of Catalonia, Barcelona, Spain*

<sup>i</sup>*Met Office, Exeter, United Kingdom*

---

## Abstract

Irrigation in semi-arid regions induces thermal heterogeneity across a range of spatial scales that impacts the partitioning of energy at the surface, the development of the atmospheric boundary layer, and the bi-directional interactions between the atmosphere and the surface. In this analysis, we use data from the Land Surface Interactions with the Atmosphere in the Iberian Semi-Arid Environment (LIAISE) experiment combined with a coupled land-atmosphere model to understand the role of the scales of irrigation-induced, thermal heterogeneity on the surface fluxes and consequently, the development of the diurnal convective boundary layer. The surface heterogeneity is characterized by Bowen ratios that range from  $\sim 0.01$  in the irrigated areas to  $\sim 30$  in the non-irrigated areas; however, the observed boundary-layers dynamics in both loca-

---

\*Corresponding author

*Email address:* maryrose.mangan@wur.nl (Mary Rose Mangan)

tions are similar. In this analysis, we address the questions of how the surface fluxes impact the development of the boundary-layer dynamics and how the boundary layer influences the diurnal cycle of surface fluxes. To interpret the observations, we introduce a heterogeneity scaling scheme where length scales range from local scale ( $\sim 100$  m) to regional scale ( $\sim 10$  km) to investigate the role of scale on surface representation in numerical models and to address the discrepancy between surface observations and their representation in weather and climate models.

We find that at the surface, both the available energy and its partitioning depend on spatial scale. The observed boundary-layer properties can be explained through the composite of surface fluxes at the regional scale. Surface fluxes at the local scales are unable to replicate the observed boundary layer – even when including large-scale contributions. We find that non-local boundary layer processes like advection are important for partitioning energy at the local scale. We explore the connection between surface fluxes and the development of the boundary layer and the potential non-local effects on boundary-layer development.

*Keywords:* Surface Heterogeneity, Scaling Surface Fluxes, Boundary-Layer Dynamics, Heat & Moisture Advection

---

## 1. Introduction

The Earth’s surface is highly heterogeneous over a variety of spatial scales, which presents a challenge for interpreting the physical processes that govern both the partitioning of energy at the surface and the development of the atmospheric boundary layer. Historically, land-atmosphere interactions have been studied by observing the one-directional impact of the surface on the atmosphere, or vice versa. Recently, there has been an effort to advance observations of land-atmosphere interactions by co-locating surface flux stations with continuous boundary-layer observations (Beamesderfer et al., 2022; Helbig et al., 2021). By coupling surface flux observations with boundary-layer observations, we can disentangle processes that govern land-atmosphere dynamics. Although Beamesderfer et al. (2022) and Helbig et al. (2021) call for long-term measurement sites for quantifying land-atmosphere interactions, intensive and comprehensive experimental campaigns provide insight on the bidirectional land-atmosphere feedbacks across spatial scales. Therefore, we use data from the Land Surface Interactions with the Atmosphere over the Iberian Semi-Arid Environment (LIAISE) campaign (Boone et al., 2021)

15 to investigate both the bidirectional land-atmosphere interactions in a thermally heterogeneous  
16 environment.

17 In this analysis, we address how the impacts of heterogeneity are felt across spatial scales.  
18 We are motivated both by process understanding of the bi-directional feedbacks between the  
19 surface and the boundary-layer and examining the usefulness of applying an idealized mixed-  
20 layer model to a heterogeneous area. Therefore, we aim to address the following questions about  
21 process understanding for the LIAISE campaign: (1) How does the thermally heterogeneous  
22 surface control the boundary-layer dynamics across spatial scales, and (2) What is the impact of  
23 the boundary-layer dynamics on the diurnal variability of the observed surface fluxes? Although  
24 the study is motivated by physical process understanding of land-atmosphere interactions, the  
25 methodology is motivated by the need to address the mismatch between how observations and  
26 models represent the physical world. We introduce a site-specific framework for modelling  
27 the scales of surface heterogeneity, which could be applied systematically to other regions to  
28 investigate the role of the scale of surface heterogeneities on the ABL. In idealized boundary-  
29 layer models low resolution limits the representation of the land surface and the atmospheric  
30 boundary layer. By comparing the impacts of the resolution of the heterogeneities between  
31 measurements and models, we can evaluate more comprehensively the parametrizations of land  
32 surface models in heterogeneous areas.

33 Because land-surface models consider subgrid scale surface heterogeneity by making a com-  
34 posite of either the land surface properties within the grid cell (parameter aggregation) or the  
35 fluxes above the surface from separate non-interacting tiles (flux aggregation), there is a discrep-  
36 ancy between the land surface modeling community’s needs and the measurements of surface  
37 fluxes. Land-atmosphere exchange has been measured by eddy-covariance systems for decades  
38 (Swinbank, 1951; Baldocchi et al., 1988; Helbig et al., 2021), and it remains one of the most  
39 common observational sources for verification of land surface models. Although through net-  
40 works like FluxNet (Baldocchi et al., 2001) and ICOS (Kadygrov et al., 2015), there is high  
41 global coverage of surface flux measurements, each eddy-covariance system measures fluxes  
42 with a relatively small footprint. This means that each tower measures the fluxes from a small  
43 area within the grid cell of the global scale model. Moreover, eddy-covariance towers typically  
44 measure below the first model level of a weather or climate model. For these reasons, measured  
45 surface fluxes do not necessarily represent the same flux that land surface models aim to repro-  
46 duce; however, these eddy-covariance systems are commonly used as model verification for the  
47 land surface models. To address the spatial disparity between the measurements and models,  
48 we created maps of surface fluxes and properties (Section 4.1) to replicate the surface and its  
49 fluxes at a regional spatial scale.

50 There have been multiple studies with large-eddy simulation and with experimental cam-  
51 paigns to quantify the impacts of surface heterogeneities on the atmospheric boundary layer.  
52 Large-eddy simulations have been used to study heterogeneity scaling in the convective bound-  
53 ary layer (Patton et al., 2005; Shen and Leclerc, 1994, 1995; van Heerwaarden et al., 2014),  
54 quantifying regional scale impacts of surface heterogeneity including secondary circulations  
55 (Raasch and Harbusch, 2001), and the development of an internal boundary layer (Bou-Zeid

56 et al., 2004). In addition to large-eddy simulation, field campaigns which include observations  
57 that span scales of heterogeneity have been used to study heterogeneous land surfaces, includ-  
58 ing the recent CHEESEHEAD experiment (Butterworth et al., 2021), the BLLAST experiment  
59 (Lothon et al., 2014), and the CloudRoots Campaign (Vilà-Guerau de Arellano et al., 2020).  
60 Nonetheless, it remains difficult for field measurements to span the same scales as the surface  
61 heterogeneity; therefore, modeling experiments have been used to connect the local scale mea-  
62 surements in heterogeneous regions to their mesoscale impacts on the boundary layer.

63 To support the interpretation of multi-scale observations from the LIAISE experiment, we  
64 used numerical experiments performed by a conceptual mixed-layer model (CLASS) (Vilà-  
65 Guerau de Arellano et al., 2015). In so doing, we could study the dominant processes at each  
66 scale and study whether new and emerging processes become dominant at different scales.  
67 We have deliberately chosen a conceptual, coupled land-atmosphere model for this study to  
68 reduce the complexities of the LIAISE domain so that we investigate the essential processes that  
69 govern land-atmosphere interactions in the thermally heterogeneous environment. Furthermore,  
70 it allowed us to replicate systematically how a land surface model handles subgrid scale surface  
71 heterogeneity at different spatial resolutions.

72 The paper is structured as follows. In Section 2, we will introduce the LIAISE campaign as  
73 it is suited for our multi-scale analysis due to the strong contrast of surface properties. We sub-  
74 sequently propose a spatial scaling scheme to represent local, landscape and regional processes  
75 (Section 3). In this way, we can replicate how a land surface model handles heterogeneous land  
76 surfaces depending on scales, and how these scales translate to a model grid cell. Next, we will  
77 describe our methods to upscale our measurements to represent each model scale, and we will  
78 describe how we replicate spatial heterogeneity using a zeroth-order model (Section 4). We will  
79 show the results from the conceptual model with the measurements and the ERA5 reanalysis  
80 model (Section 5). Finally, we will bring the scales together to discuss the bidirectional impacts  
81 between boundary-layer dynamics and surface fluxes in a heterogeneous environment (Section  
82 6).

## 83 **2. Experimental and Modeling Approach**

84 In this study, we used data from the LIAISE campaign and a mixed-layer coupled land-  
85 atmosphere model to investigate surface fluxes at different scales of heterogeneity. Results from  
86 observations and the mixed-layer model were compared to the 0.25° resolution European Centre  
87 for Medium-Range Weather Forecasts’ (ECMWF) reanalysis product, ERA5 (Hersbach et al.,  
88 2020). We use ERA5 as a prototypical ABL for the modeling efforts because its land surface  
89 model partitions energy in a similar way as the CLASS model. In this way, we can make a direct  
90 comparison between our modeling study and how global models handle surface heterogeneity,  
91 especially at the regional scale where the horizontal domain matches that of ERA5.

### 92 *2.1. Site Description: LIAISE Domain*

93 The LIAISE field campaign took place in the Ebro River Valley in Catalonia, Spain during  
94 May through October 2021. The LIAISE experiment was designed to improve understanding

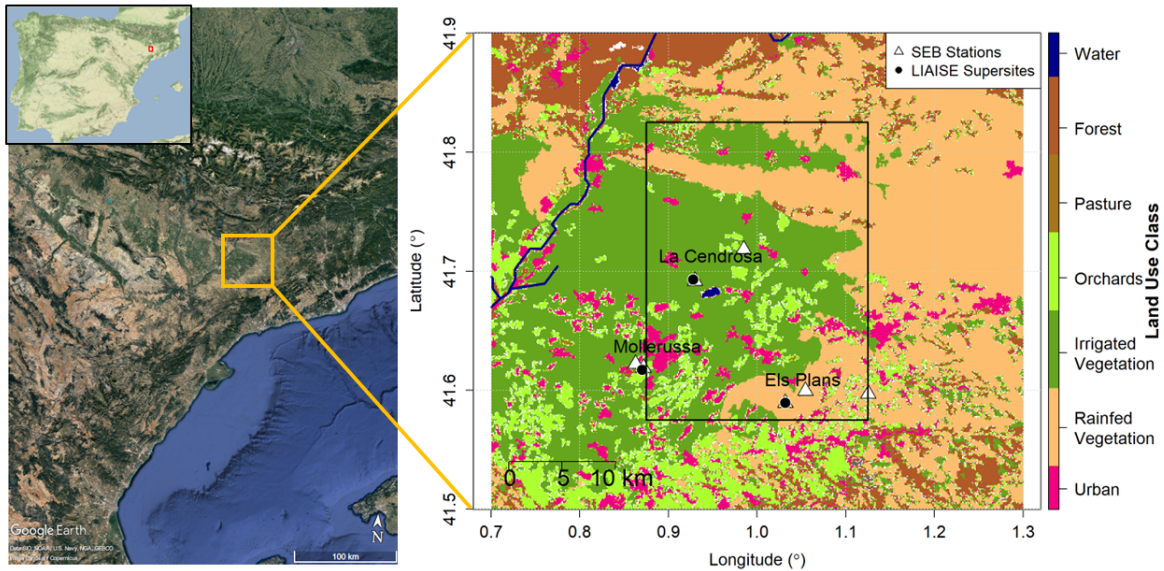


Figure 1: The LIAISE campaign occurred in the Ebro River Valley in Northeast Spain in the summer of 2021. The left panel show the aerial view of the LIAISE domain (image from GoogleEarth). The inset in the left picture is the location of the experimental site in the Iberian Peninsula. The right panel is the 100 m land cover map from CORINE Land Cover Product (Buttner, 2014). The box in the land use map is the extent of the ERA5 grid cell in the LIAISE domain.

95 of land-atmosphere interactions in a thermally heterogeneous environment (Boone et al., 2021,  
 96 2019). Atmospheric flow in the LIAISE domain is complex for three reasons: (1) it is located  
 97 in a nearly closed valley in the Ebro River Basin, (2) the Mediterranean Sea is located approxi-  
 98 mately 70 km to the southeast which induces a land-sea circulation, and (3) within the LIAISE  
 99 domain, there is a strong thermal heterogeneity (Fig. 1). Fig. 1 indicates the land use classes  
 100 in the LIAISE study domain. The western part of the domain contains annual, irrigated crops  
 101 like maize and alfalfa and irrigated fruit trees. The eastern part of the domain contains rainfed  
 102 vegetation consisting mainly of winter cereal crops, vineyards and rainfed orchards. The box  
 103 inside of right plot in Fig. 1 represents the extent of the ERA5 grid cell in the LIAISE domain.

104 For the purposes of our study, we were most interested in the thermal heterogeneity within  
 105 the LIAISE domain that arises from irrigation applied in one area with a length scale on the or-  
 106 der of 10-100 km. There were measurements in a number of locations near the sharp boundary  
 107 between the irrigated and the semi-arid areas. In the LIAISE campaign, there were three "super-  
 108 site" locations: Mollerussa (mixed orchards), La Cendrosa (alfalfa field) and Els Plans (fallow  
 109 field with rainfed, natural vegetation) (Fig. 1). In addition to the three supersites, there was a  
 110 network of nine surface energy budget (SEB) stations in each of the predominant crop types  
 111 in the LIAISE domain. All measurement locations were located within 10 km of the wet-dry  
 112 boundary.

## 113 2.2. *Experimental Data: LIAISE Campaign*

114 The LIAISE field campaign included a short-term observation period from 15 July through  
115 30 July 2021. At Els Plans (rainfed fallow) and La Cendrosa (irrigated alfalfa), measurements  
116 spanned scales from the leaf level to the boundary-layer level. Data collected at each supersite  
117 include ecophysiology measurements, SEB stations and boundary-layer measurements includ-  
118 ing 50 m towers, tethered balloons and hourly radiosondes during the daytime. Across the entire  
119 LIAISE domain, there were aircraft measurements of the boundary layer (e.g., turbulent fluxes)  
120 and the surface (e.g., solar induced fluorescence and soil moisture). Additionally, there was  
121 a network of nine SEB stations in the predominant vegetation covers in the LIAISE domain.  
122 For more information about the extent of the measurements from the LIAISE experiment, see  
123 Boone et al. (2021).

124 In Table 1, we show the overview of the data used in this study. At the surface, we used  
125 data from the network of the nine SEB stations and the lowest level of flux measurements at  
126 Els Plans (2 m) and La Cendrosa (3 m). At the surface stations, there were eddy-covariance  
127 systems, four-stream radiometers and ground heat flux measurements. The sampling times for  
128 the systems varied from 10-20 Hz for the eddy-covariance to 60 seconds for the radiative fluxes,  
129 however, all SEB data was block averaged to 30 minutes. The fetch during convective condi-  
130 tions for the surface stations varied from 50 to 150 m downwind, depending on the measurement  
131 and crop heights, which fell within the field boundaries in the predominant wind direction for  
132 all fields. For boundary-layer measurements, we used hourly radiosondes where we derived the  
133 boundary layer height with the parcel method (Kaimal and Finnigan, 1994), the mixed-layer  
134 mean potential temperature and specific humidity and the entrainment jumps in the potential  
135 temperature and specific humidity at the top of the boundary layer (Fig. 1 Conzemius and Fe-  
136 dorovich, 2007; Driedonks and Tennekes, 1984). The mixed-layer scalar means were calculated  
137 with the average of the radiosonde values of potential temperature and specific humidity below  
138 the mixed-layer height. The entrainment jumps in scalars were found by first determining the  
139 lapse rate of the scalar in the free atmosphere. Using that lapse rate, we extrapolated it to find  
140 the expected value at the top of the mixed-layer. The jump is defined as the difference between  
141 the value at the mixed-layer top and the mean mixed layer value. Finally, we used data from the  
142 automated weather stations, which will be explained in more detail in Section 4.1.

143 We averaged a three day period from 20 July through 22 July to represent a “composite  
144 day” of the LIAISE experiment. Both the synoptic situation and the surface fluxes were similar  
145 over this period. There was anticyclonic flow at the surface with a thermal low building to the  
146 west of the study site. Over the course of this three day period, local conditions in the LIAISE  
147 domain were slowly getting hotter and drier. For these reasons, we created a composite LIAISE  
148 composite day by taking the average of the surface fluxes and boundary-layer properties over  
149 20-22 July for use in the mixed-layer model. By using a composite composite day, we were able  
150 to better capture a typical situation for the LIAISE domain instead of modeling a situation that  
151 was heavily infused by random extremes due to measurement limitations or non-local events.  
152 Furthermore, creating a composite day allowed us to have a robust procedure for handling  
153 missing data.



Table 1: An overview of the data from the LIAISE field campaign used in this study including the nominal sampling time and the averaging time.

	Instrument	Derived Variable	Locations	Sampling Frequency	Averaging Time
<b>Surface - Fluxmaps</b>					
Sonic Anemometers	Campbell Sci. CSAT3	H	9	10-20 Hz	30 min
	Gill WindMaster R.M. Young 81000				
Gas Analyzers	Campbell Sci. Irgason EC150	LE	9	10-20 Hz	30 min
	LICOR-7500 Krypton KH2O				
Radiation	Hukseflux NR-01 Kipp & Zonnen CNR4	$R_n$	9	1 - 60 s	30 min
Surface Heat Flux	Hukseflux HFP01	G	9	1 - 60 s	30 min
<b>Boundary Layer</b>					
Radiosondes	Vaisala RS92-SGP	$h, \theta, q$	2	1 hour	
<b>Meteorological Stations</b>					
AWS	Vaisala HMP155 R.M. Young 05103	$T_{2m}, q_{2m}$ $U_{10m}$	15	1 min	30 min

At both La Cendrosa and Els Plans, there were SEB stations which directly measure the components of the energy budget: net radiation ( $R_n$ ), sensible heat flux ( $H$ ), latent heat flux ( $LE$ ), ground heat flux ( $G$ ). The average energy budget non-closure from 7 to 17 UTC at these sites varied from 33% in La Cendrosa to 15% in Els Plans. We forced energy budget closure using the method from Twine et al. (2000), which preserves the observed Bowen ratio, for comparison with the CLASS model. Additionally, there were measurements of three-dimensional wind, temperature, humidity, air pressure, soil temperature and soil moisture. Boundary-layer measurements at both sites include a 50 m tower with three-dimensional wind, temperature and moisture measurements at 10, 25 and 50 m above ground level. Moreover, at both sites, there were hourly radiosondes launched starting at 06:00 LT (UTC+2) through 19:00 LT during all three of the composite days. Ecophysiological measurements, including stomatal conductance,  $CO_2$  and light-response curves, and leaf-area index were taken at La Cendrosa on 17 and 19 July.

To demonstrate the contrast between the irrigated and rainfed areas, we show Fig. 2 which includes the diurnal cycle of the surface energy balances for both Els Plans and La Cendrosa during the composite day and the radiosondes launched in both sites at 15:00 LT (UTC+2). Hereafter, all of the time series will be presented in UTC instead of local time (UTC+2) because in the study domain, solar noon is approximately 12 UTC. In Fig. 2a and 2b, the surface energy balances for La Cendrosa and Els Plans are displayed. The observed albedo between the two sites were comparable ( $\alpha \approx 0.23$ ), but the surface temperature, and therefore, outgoing longwave radiation was higher for Els Plans than for La Cendrosa, so there was more available energy at La Cendrosa than Els Plans. Much of the available energy at La Cendrosa was par-

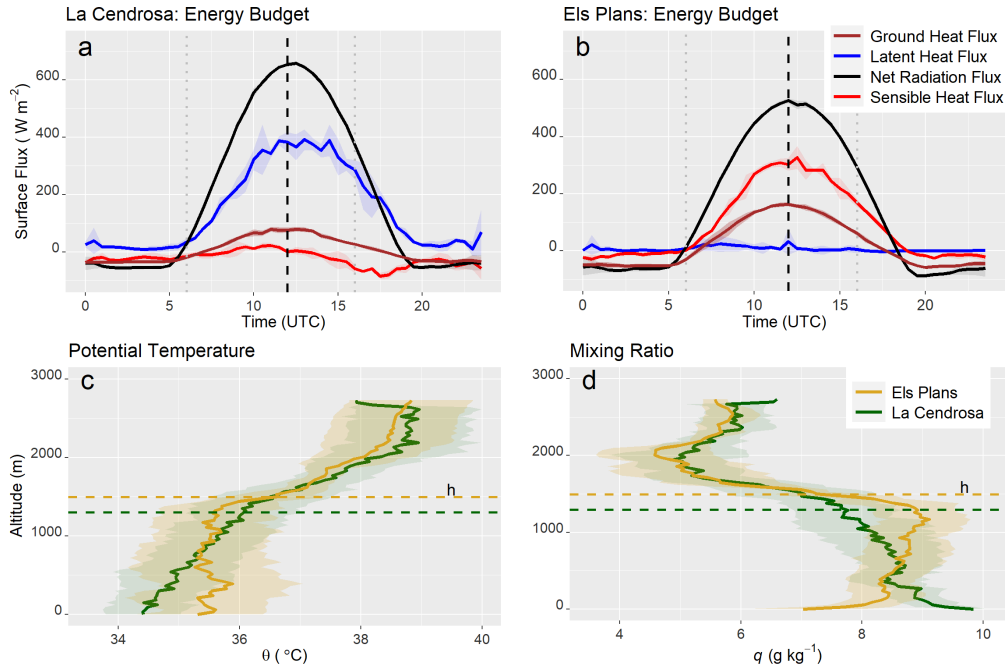


Figure 2: LIAISE Composite composite day: 20-22 July 2021. (a) The surface energy balance for La Cendrosa averaged across composite day, and (b) The surface energy balance for Els Plans averaged across the composite day. (c) Potential temperature from a radiosonde launched at 13:00. (d) specific humidity measured from the radiosondes launched at 13:00 during the composite day. In all subsequent figures, the solid line is the mean for all composite day and the shaded area represents one standard deviation from the mean.

176 titioned into latent heat flux, and the observed sensible heat flux became negative after 13:00  
 177 UTC which indicates stable conditions in the surface layer. Conversely, at Els Plans, much of  
 178 the available energy was partitioned into sensible heat flux, while latent heat flux remained near  
 179 zero the entire day. In Fig. 2c and 2d, the potential temperature and specific humidity measured  
 180 via radiosondes were averaged together from 13:00 UTC during the three days. At La Cendrosa  
 181 (green), the surface was cooler and wetter than at Els Plans (yellow), but Els Plans had a better  
 182 defined mixed-layer. The boundary-layer heights were approximately the same regardless of  
 183 land cover; however, we observe a thin stable boundary-layer in the lowest  $\sim 200$  m at La Cen-  
 184 drosa. Furthermore, we observe that above 500 m, there is dry air intrusion in the La Cendrosa  
 185 radiosonde above the locally wet surface layer, while the Els Plans radiosonde shows a well-  
 186 mixed profile. This supports the idea that there is a blending height above which the influence  
 187 of the landscape scale diminishes, as suggested in Fig. 3.

### 188 2.3. Coupled Land-Atmosphere Model

189 We used the atmospheric mixed layer, slab model Chemistry Land-surface Atmosphere Soil  
 190 Slab model (CLASS) (<https://classmodel.github.io/>; Vilà-Guerau de Arellano et al. (2015)) to  
 191 help us interpret the LIAISE composite day. By using a coupled land-atmosphere mixed-layer

192 model, the complexities of the LIAISE campaign can be simplified such that topography and  
193 advection were prescribed. To further disentangle the situation, we were interested mainly in  
194 the daytime before the sea breeze arrives in the LIAISE domain. The sea breeze arrives between  
195 14:30 and 15:45 UTC during the composite day. Although we show the results of the model  
196 until 18:00 UTC, our discussion is focused on processes that occur before the arrival of the sea  
197 breeze. By using this model, we could delineate the bi-directional impact of the land surface on  
198 the atmosphere and the atmosphere on the land-surface fluxes.

#### 199 *Land Surface Representation*

200 The surface layer model was based on Monin-Obukhov similarity theory. At the land sur-  
201 face, the vegetation was represented by a big-leaf model, where the partitioning of energy was  
202 done with the Penman-Monteith equation. We used the Jarvis-Stewart land-surface model to  
203 parameterize the vegetation surface resistance (van Heerwaarden et al., 2009). The evolution of  
204 both soil moisture and temperature used the force-restore method (Noilhan and Mahfouf, 1996;  
205 Noilhan and Planton, 1989).

206 The land surface was represented in the CLASS model with static variables – like leaf area  
207 index ( $LAI$ ), vegetative fraction ( $c_{veg}$ ), and soil moisture. Most of the variables to describe the  
208 land surface are consistent between the scales. For example, we assumed that the soil properties  
209 including wilting point and field capacity are relatively constant throughout the domain. Soil  
210 properties were estimated using soil maps from Institut Cartogràfic i Geològic de Catalunya  
211 (2009-2020). Soil thermal conductivity was used as a tuning parameter for capturing the ground  
212 heat flux for each scale. Initial surface temperature were taken from observations from the early  
213 morning. The variables to describe the land surface were determined by creating surface maps  
214 which are described in more detail in Section 4.

215 The CLASS model had two soil layers: the top one which responded to the atmosphere  
216 dynamically, and the bottom one which represented the root zone. In the bottom, reservoir  
217 soil layer, the temperature and moisture were constant throughout the day. There was slow  
218 diffusion of heat and moisture from the reservoir soil layer to the top soil layer. In this analysis,  
219 the reservoir soil layer had soil moisture that is set to field capacity for all scales, and the top  
220 soil layer is set to observed values at each scale. This means that the top soil layer controls  
221 the surface evaporation and the partitioning of energy at the surface, and the reservoir soil layer  
222 controls plant transpiration. Thus, the plants modeled with CLASS are never water stressed.  
223 In the dry scales, where plants were likely water stressed, this effect was taken into account by  
224 altering the vegetative cover (Section 4.3).

#### 225 *Mixed Layer*

226 In the CLASS model, the mixed layer prognostic model was described by Tennekes (1973).  
227 Initial conditions for mixed-layer characteristics (e.g. potential temperature, specific humidity,  
228 mixed-layer height) were prescribed based on the mean radiosondes from the composite day  
229 (see Section 4.2). The model calculated the time-evolving mixed-layer properties every five  
230 seconds. For example, the potential temperature ( $\theta$ ) was calculated with

$$\frac{\delta\theta}{\delta t} = \frac{\overline{w'\theta'} - \overline{w'\theta'_e}}{h} + adv_\theta \quad (1)$$

231 where  $\overline{w'\theta'}$  is the surface heat flux,  $\overline{w'\theta'_e}$  is the entrainment heat flux and  $adv_\theta$  is the temperature  
 232 advection, and  $h$  is the mixed-layer depth. The surface fluxes impacted the heating (and moist-  
 233 ening) of the mixed-layer, as well as the growth of the mixed-layer. In turn, the mixed-layer  
 234 properties controlled the gradient between the surface and the atmosphere which impacts the  
 235 surface fluxes.

236 The LIAISE domain was characterized by its different scales of heterogeneity, so a modeling  
 237 scheme was developed to reflect these scales (see Section 3). The CLASS model is single  
 238 column slab model with added advection, so each spatial scale is represented by one vertical  
 239 column where the surface conditions are changed to reflect the composite land cover at that  
 240 scale. The CLASS model incorporated larger scale forcing by including advection terms for  
 241 momentum, temperature and moisture (Vilà-Guerau de Arellano et al., 2015, 2020). In order  
 242 to better capture the observed boundary layer in the CLASS model runs, large scale advection  
 243 of temperature and moisture were included based on a network of Automated Weather Stations  
 244 (AWS) operated by the Servei Meteorològic de Catalunya. More information on this procedure  
 245 can be found in Section 4.2.

### 246 3. Spatial Scaling Scheme

247 In the LIAISE domain, surface heterogeneities occur across a range of spatial scales. We  
 248 have defined three scales of heterogeneities in order to compare the results of the mixed-layer  
 249 model with the surface fluxes that were constructed from local measurements during the LIAISE  
 250 campaign. In this way, we can both quantify the impact of scale on modeled and measured  
 251 fluxes and evaluate how the surface fluxes impact the development of the boundary layer across  
 252 each scale. We have defined three scales: regional ( $\sim 10$  km), landscape ( $\sim 1$  km) and local  
 253 ( $\sim 100$  m). The regional scale consists of wet and dry landscape scales, and within the landscape  
 254 scale, there are alfalfa and fallow local scales to represent individual fields. Existing methods to  
 255 characterize heterogeneities focus on size of the heterogeneity (van Heerwaarden et al., 2014) or  
 256 the structure of the heterogeneity (Bou-Zeid et al., 2020); however, much of the scaling research  
 257 has been focused on one scale or type of heterogeneity – not how the type of heterogeneity  
 258 depends on the scale.

259 The largest scale in the LIAISE domain is the regional scale, which has a length scale  
 260 on the order of 10s km. On this scale, the heterogeneity is from a large, single wet patch  
 261 surrounded by dry land. This scale represents the extent of the ERA5 grid cell that is shown  
 262 in Fig. 1. This is classified as a Type III – large individual patch class of heterogeneity by  
 263 Bou-Zeid et al. (2020). Within the regional scale, there are landscape scales within both the  
 264 wet and the dry patches each with a length scale on the order of 1 km. Within this scale,  
 265 there are heterogeneities between fields – in both moisture and surface roughness. This type of  
 266 heterogeneity is considered Type IV unstructured heterogeneity as defined by Bou-Zeid et al.

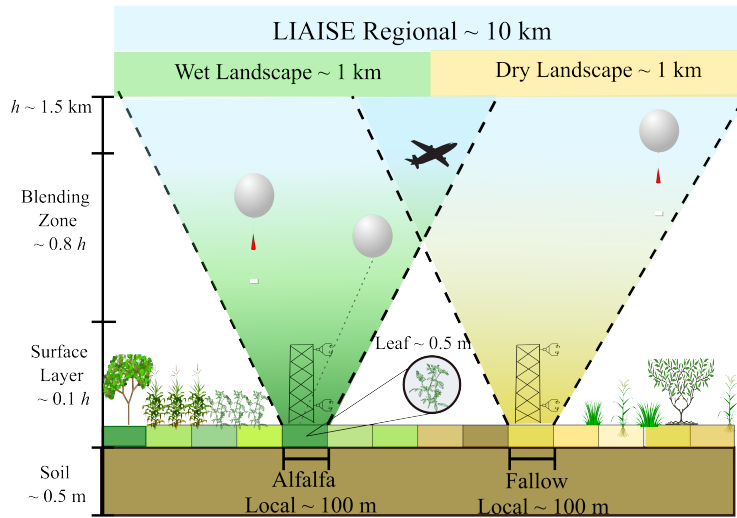


Figure 3: The schematic representation of the scales in the LIAISE and how they interact with each other with height in the atmospheric boundary layer. The local scale impacts the surface layer. Above the surface layer, there is a blending zone which is most impacted by the landscape scale. Above the blending height, the regional scale controls the boundary layer. The LIAISE campaign has instrumentation to measure with height in the boundary layer: flux towers measure in the surface layer, tethered balloons measure in the blending zone, and radiosondes and aircraft measure above the mixed layer.

267 (2020). The smallest scale is the local scale, which is on the order of 100 m. It represents  
 268 individual fields: La Cendrosa alfalfa for the irrigated (alfalfa) local scale and Els Plans natural  
 269 vegetation for the dry (fallow) local scale. We assume that the local scale is a statistically  
 270 homogeneous area. We propose our scaling scheme to be complementary to the one proposed  
 271 by van Heerwaarden et al. (2014) in which they defined heterogeneity scaling as macroscale,  
 272 mesoscale or microscale depending on the size of the heterogeneous patch compared to the  
 273 domain. The regional scale is a macroscale heterogeneity, the landscape scales are mesoscale  
 274 heterogeneities and the local scales are microscale heterogeneities.

275 Fig. 3 is an abstract representation of the horizontal scales and how they interact with each  
 276 other in the boundary layer. The impact of the local scales are felt near the surface. The land-  
 277 scape scales, which capture the heterogeneity between fields in both the irrigated and rainfed  
 278 areas, are felt above the surface layer where impacts from local fields are blended together.  
 279 Above the blending height near the top of the boundary layer, the impacts of the regional scale  
 280 are felt in the atmosphere. Depending on the type of measurements, we observe fluxes that are  
 281 representative of different scales. These are the first-order effects: each horizontal scale feeds a  
 282 vertical scale in the atmosphere. The second-order effect is that the vertical scales interact with  
 283 each other in the boundary layer and communicate downwards to impact the surface fluxes.

284 In order to replicate the spatial scales using the single pixel mixed-layer model, we defined a  
 285 composite land surface for each scale based on a spatial average of surface characteristics. This

286 is analogous to the parameter aggregation scheme used in land surface models. We imposed  
287 the calculated advection term in the local scale cases to replicate the boundary layer. We will  
288 discuss the observational data preparation that was necessary to replicate these scales both in  
289 the CLASS model and with observational data in the next section.

## 290 **4. Data Integration and Upscaling**

291 In order to evaluate the behavior of the CLASS model representative of different spatial  
292 scales, we needed to upscale the surface fluxes and surface properties, measured at local scales,  
293 to match the regional and landscape scales. The purpose of this data integration is to combine  
294 networks of measurements to estimate a spatial distribution of surface properties and fluxes. By  
295 upscaling the data, we could directly compare measurements to both the CLASS and ERA5  
296 models. In this section, we introduce the mixed layer properties and surface parameters that  
297 constrain the CLASS model. We also introduce the data products that are used to verify the  
298 model.

299 In Section 4.1, we describe the data used to constrain and verify the land surface representa-  
300 tion in CLASS. We describe the upscaling of surface flux data to represent surface fluxes across  
301 the regional and landscape scales. By representing the land surface as a composite of realistic  
302 surface, we are using parameter aggregation to describe the heterogeneity, but we are verify-  
303 ing the product with flux maps, which represents the flux aggregate approach to describe the  
304 heterogeneity. In Section 4.2, we describe the data approach for constraining the mixed layer.  
305 We introduce an approach to calculate boundary-layer advection from a network of automatic  
306 weather stations so that we can replicate the boundary layer at the local scales. In Section 4.3,  
307 we summarize the data approach and outline the experimental design based on spatial scale.

### 308 *4.1. Land Surface Data: Surface Maps*

309 To create the land surface differences between the scales, we adjusted vegetation properties  
310 and the top layer of soil moisture based on observations. The spatially aggregated land surface  
311 constrains the CLASS model. We used the diurnal cycle of observed surface energy budget  
312 components to verify the model. In order to prepare the input land surface parameters and  
313 the surface energy budget data for model verification for the regional and landscape scales,  
314 we created surface flux and representation maps. Using these maps, we created a dataset that  
315 represents the mean surface properties at the landscape and regional scales.

316 The LIAISE campaign included a network of SEB stations across the predominant crop  
317 types in the area during the summertime. In total, there were nine different SEB stations used  
318 for this analysis, including stations located in alfalfa, maize and fallow fields, fruit, and nut  
319 orchards, and a vineyard. All SEB stations were processed uniformly using EddyPro (LI-COR  
320 Biosciences; (Fratini and Mauder, 2014)). We gap-filled the data using available data from the  
321 other composite days. In addition to uniform processing of the network of eddy-covariance  
322 stations, a 100 m resolution land cover map from the Sistema de Información Geográfica de  
323 Parcelas Agrícolas (SIGPAC) was used to provide the spatial extent of the crops. The SIGPAC

324 crop cover map was supplemented by the 100 m CORINE Land Cover product for the urban  
325 areas and the water bodies (Buttner, 2014) (see Fig. 1). Crop types for SIGPAC were reclassified  
326 to match those of the predominant vegetation types from the SEB station network. Measured  
327 fluxes were applied to the corresponding crop type within the LIAISE region to create flux maps.  
328 See Appendix A for more information on the reclassification method for the SIGPAC crop cover  
329 maps. Although the 2020 crop cover map was used, we assume that the total distribution of crop  
330 types is similar between 2020 and 2021.

331 At the regional scale, 21.3% of the land area was urban. Because there were no SEB sta-  
332 tions in an urban area in the LIAISE campaign, we modeled the expected surface fluxes using  
333 the method described in Román-Cascón et al. (2021). We assumed that the urban land had a  
334 Bowen ratio ( $\beta$ ) of 5, an emissivity of 0.92 and an albedo of 0.15 (Grimmond and Oke, 1999;  
335 Lemonsu et al., 2004).  $G$  was assumed to be 10% of  $R_n$  during daytime. Fluxes of sensible and  
336 latent heat flux were solved by iteratively updating surface temperature using measured incom-  
337 ing shortwave radiation, air temperature, humidity observed at the grass SEB site. The same  
338 procedure was used for the fluxes over a water surface (which accounts for 0.3% of the regional  
339 surface area). In that case, the assumed  $\beta$  was 0.1, an emissivity of 0.98 and an albedo of 0.08.  
340  $G$  was assumed to be 30% of  $R_n$  during daytime.

341 Fig. 4 displays an example of the flux maps for latent heat flux for the LIAISE domain  
342 on 20 July 2021 at 14:00 UTC. The entire map represents the LIAISE regional scale. The  
343 dashed line is the separation between the wet and dry landscape scales. The regional fluxes  
344 were calculated as a spatial average of the fluxes in the entire domain, and the wet and dry  
345 landscape fluxes were calculated as a spatial average from the area inside and outside of the  
346 dashed line in Fig. 4 respectively. Consequently, we were able to derive time series of regional,  
347 dry and wet landscape scale energy budget components.

348 In the wet landscape, the latent heat flux was as high as  $400 \text{ W m}^{-2}$ , but this depends  
349 on the crop cover at the local scale. Within the wet landscape scale, there were urban areas  
350 near Mollerussa which provide relatively high sensible heat flux compared to the rest of the  
351 landscape. In the dry landscape, the fields that were fallowed in the summer, like Els Plans, had  
352 high Bowen ratios. The orchards in the dry landscape provided more latent heat flux compared  
353 to the rest of the landscape. There were maize fields in the north of the LIAISE region, which  
354 moistened the dry landscape scale. Within the landscape scales, it is evident that there can be  
355 strong differences between fields.

356 In addition to using the land cover map to create flux maps for the components of the surface  
357 energy balance, we have created maps based on the ecopsychological measurements to estimate  
358 vegetative properties at the landscape and regional levels, including  $LAI$ ,  $c_{veg}$ , and stomatal  
359 conductance, which are used to prescribe the surface at the regional and landscape scales. See  
360 Appendix A for more details about the flux and surface map products.

#### 361 4.2. Mixed Layer Data: Model Initialization & Advection

362 Unlike the input parameters for the land surface representation of the CLASS model, the  
363 mixed-layer properties change during the day. We inputted mixed-layer characteristics (e.g.

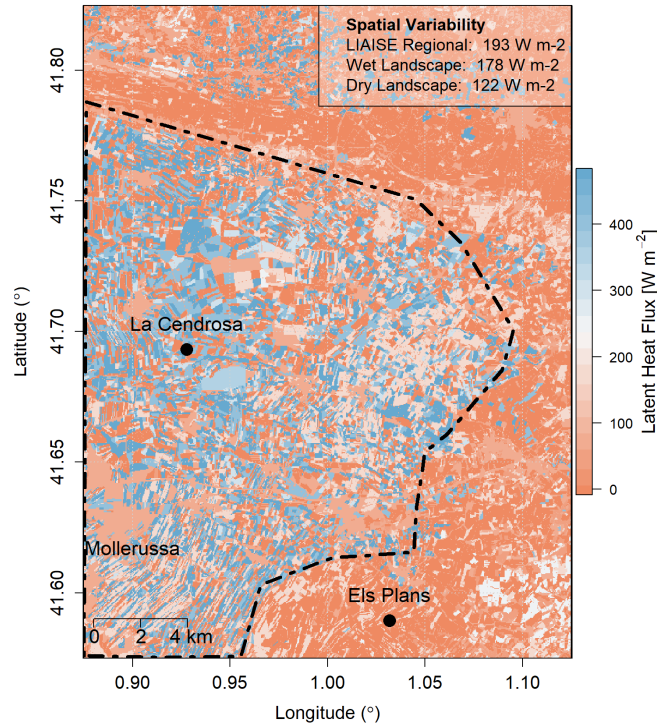


Figure 4: An example flux map for latent heat flux for 20 July 2021 at 14:00 UTC. The dashed line represents the boundary between the wet and dry landscape scales. The total grid cell represents the LIAISE regional scale as well as the ERA5 grid ( $0.25^\circ \times 0.25^\circ$ ) cell for the LIAISE domain. The dashed line represents the separation between the wet (west) and dry (east) landscape scales. The local scales are represented by the points at La Cendrosa (alfalfa local) and Els Plans (fallow local) respectively. The box in the top right corner has the spatial standard deviation for each spatial scale.

364 mean mixed-layer potential temperature, mean mixed-layer specific humidity and mixed-layer  
 365 height) at the start of the model run (6:00 UTC). During the LIAISE composite day, there  
 366 were hourly radiosondes between 04:00 UTC and 17:00 UTC that were launched from both La  
 367 Cendrosa and Els Plans. The radiosondes launched at 06:00 UTC at both sites were averaged  
 368 together to calculate the initial mixed-layer properties. After providing the initial conditions,  
 369 the CLASS model calculated the mixed-layer characteristics, including mean potential temper-  
 370 ature, mean specific humidity and mixed-layer height. The dynamically changing mixed-layer  
 371 characteristics were verified using hourly radiosondes from both the wet and the dry areas.  
 372 We calculated the mixed-layer height with the parcel method approach from the radiosondes  
 373 (Kaimal and Finnigan, 1994).

374 For all scales, the initial boundary-layer profile from the soundings at 06:00 UTC was used.  
 375 The CLASS model is insensitive to the initial conditions in the range the measurement uncer-  
 376 tainties after the first hour. The only difference in the mixed-layer input between scales was  
 377 the diurnal advection term. At the regional and landscape scales, there was weak advection that



378 corresponds to synoptically driven hot, dry westerlies to the region during the day. In the late af-  
 379 ternoon (after 15:00 UTC), we prescribed slightly cool and moist advection to represent the sea  
 380 breeze. At the regional and landscape scales, we assumed that the boundary-layer development  
 381 was primarily formed within the region; however, at the local scale, this weak synoptic advec-  
 382 tion was insufficient to describe the observed boundary layer. Without advection, the surface  
 383 fluxes from the alfalfa local scale yielded a boundary-layer height of  $\sim 800\text{m}$ , while the surface  
 384 fluxes from the fallow local scale yielded a boundary-layer height  $\sim 1700\text{ m}$ . This implies that  
 385 the boundary layer is not formed locally over either scale. Therefore, we have calculated ad-  
 386 vection of moisture and heat for the alfalfa and fallow local scale cases using an AWS network  
 387 operated by the Servei Meteorològic de Catalunya.

388 In order to calculate advection, we have selected fifteen AWS locations in the LIAISE do-  
 389 main (Fig. 5a). During the day, the wind direction was predominantly from the west. In the  
 390 late afternoon when the sea breeze arrives, the wind direction shifted so that it is predominantly  
 391 from the east. This means that during the day, air is advected from the hot and dry semi-arid  
 392 steppes at the center of the Ebro basin through the irrigated area. As the air is advected through  
 393 the wet landscape, the air mass moistens and cools. After the air mass is modified by the wet  
 394 landscape, then it advects over the hot and dry natural vegetation area in the LIAISE domain.  
 395 Therefore, we expect relatively warm and dry advection across the wet landscape and relatively  
 396 cool and wet advection into the dry landscape during the day. When the sea breeze arrived in  
 397 the late afternoon, it introduced cool, moist air from the sea. At that time, the air mass was  
 398 modified due to a relatively hot and dry surface. Based on these assumptions, we have select  
 399 the stations in blue and white in Fig. 5a to calculate the local advection at the alfalfa local scale,  
 400 and the red and white stations in Fig. 5a to calculate the local advection at the fallow local scale.

401 We calculated the advection using

$$adv_x = \bar{U} \frac{dX}{dr} \quad (2)$$

402 where  $\bar{U}$  is the mean wind speed,  $\frac{dX}{dr}$  is the gradient of the scalar (e.g. potential temperature  
 403 or specific humidity) between stations that align in the mean wind direction where  $dr$  is the  
 404 distance between stations. We calculated the advection between each station that falls within  
 405 the mean wind direction for each 10-minute interval and averaged them to calculate the mean  
 406 advection for both Els Plans (fallow) and La Cendrosa (alfalfa) (Fig. 5). We input the ad-  
 407 vection of heat and moisture terms hourly in the CLASS model runs, and between the updated  
 408 values, the advection terms are linearly interpolated. See Appendix B for more details about the  
 409 advection calculation using the AWS network.

410 A typical diurnal cycle of advection was calculated from an average of data for all of July  
 411 2021. We chose to use the monthly mean diurnal cycle of advection in the CLASS model  
 412 because it smoother than the advection for the composite day, but shows the same pattern and  
 413 magnitude. Fig. 5b is the mean diurnal cycles of temperature and Fig. 5c is the mean diurnal  
 414 cycle of moisture advection. The diurnal cycle of advection terms are reasonable based on the  
 415 large-scale forcing observed during the LIAISE campaign. In the wet area, there was warm and

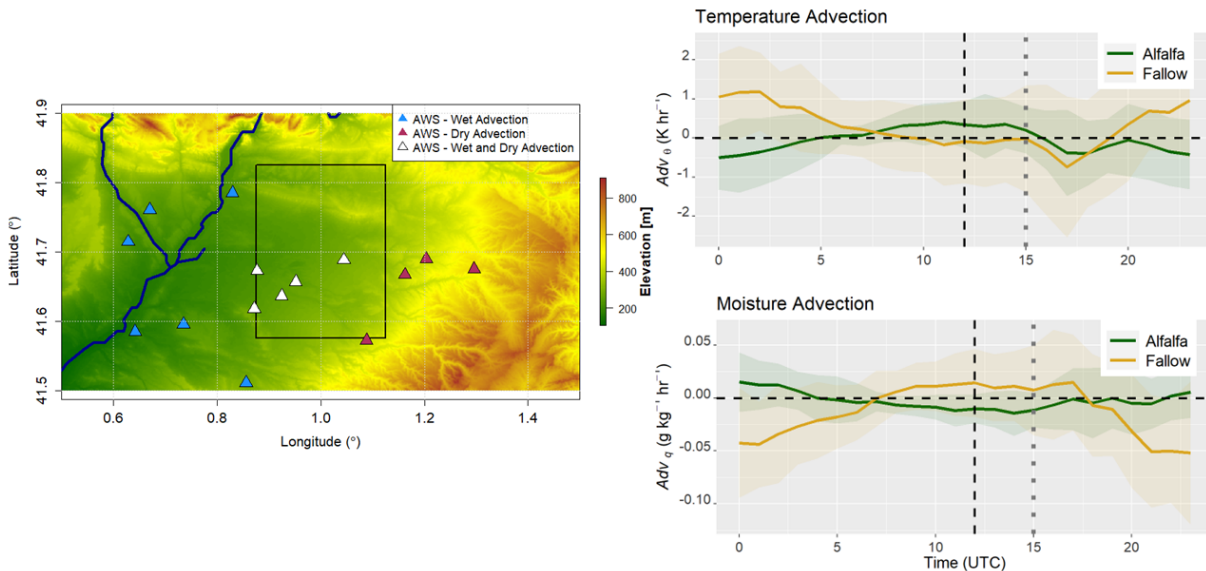


Figure 5: (a) The Automated Weather Stations from SMC used to calculate the advection in the local alfalfa and fallow fields. The blue points are stations used only for the wet advection, the red points are used only for dry advection, and the white points are stations used in both the wet and dry fields. The base map shows the elevation of the LIAISE domain above sea-level (European Digital Elevation Model, version 1.1). (b) Diurnal Cycle of temperature advection for the wet field (green) and the dry field (yellow). (c) Diurnal cycle of moisture advection for the wet field (green) and the dry field (yellow). The black dashed line indicates noon, and the gray dot-dashed line indicates the approximate time that the sea breeze starts.

416 slightly dry advection in the mid-day, as the synoptic forcing was from westerlies from inland  
 417 in the Iberian peninsula. The mid-day temperature advection across the wet-dry boundary was  
 418 not appreciable, but there was strong moist air advection. In the mid-afternoon – after 15:00  
 419 UTC – when the sea breeze arrived to the LIAISE domain, the advection terms for both the wet  
 420 and dry areas look similar. The advected air mass was cool and moist, which corresponds to  
 421 what is expected from the sea breeze.




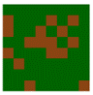






#### 422 4.3. Data Constraints and Verification for CLASS Model

423 The CLASS model cases for the scales were heavily constrained by data observed locally  
 424 and upscaled using the technique described in Section 4.1. The mixed-layer profile and the  
 425 state of the atmosphere were initialized once at 06:00 UTC. We defined the surface at each  
 426 scale using measurements from the LIAISE campaign. The mixed layer was initialized at the  
 427 start of the model run, but advection was a dynamically changing parameter. At the local scale,  
 428 we defined advection with the AWS network described in Section 4.2. At the regional and  
 429 landscape scales, advection was weak and used only as a tuning parameter to capture the sea  
 430 breeze. We assumed that there is no large-scale subsistence, because we have selected days with  
 431 weak synoptic forcing. According to ERA5, wind divergence is on the order of  $10^{-6}\ s^{-1}$ . In the  
 432 CLASS model, the subsistence velocity is defined as the wind diverge times the boundary layer

433 depth (Vilà-Guerau de Arellano et al., 2015). If we assume that the boundary layer height is on  
434 the order of 1000 m over the day, we find the subsistence velocity is on the order of  $10^{-3} \text{ m s}^{-1}$ ,  
435 which is an order of magnitude lower than the entrainment velocity. For all cases, the CLASS  
436 model was verified using either local surface fluxes or the aggregated fluxes to the landscape  
437 and regional scales for the surface performance. Hourly radiosondes launched from Els Plans  
438 and La Cendrosa were used to verify the mixed-layer model performance.

439 Table 2 summarizes the differences between the spatial scales introduced in Section 3 and  
440 how they are replicated using the CLASS model. The columns indicating scale view and model  
441 view show the spatial extent of the heterogeneity in each scale and how that is represented  
442 using  $LAI$  and  $c_{veg}$  in the CLASS model. The columns indicating the model initialization and  
443 verification focus on the differences between the scales. For the verification, the variables are  
444 the same, but the representative areas differ.

Table 2: The scale definition and numerical scheme for the conceptual model. The scale-view shows the horizontal extent of each scale. The model-view demonstrates how the model observes the land surface based on the  $LAI$  and  $c_{veg}$ . The input parameters are the ones derived from data that change between scales, while the verification parameters are dynamically changing from observations described in the "Data Source" column.

Scale	Scale-View	Model-View	Input Parameters				Verification Parameters		Data Source	
			Surface		Mixed Layer		Surface	Mixed Layer		
			$LAI$	$c_{veg}$	$SM$	$Adv$				
Regional ( $\sim 10$ km)	LIAISE			1.25	0.5	0.2	Synop.	$R_n, G$ $H, LE$	$h$ $\theta, \delta\theta$ $q, \delta q$	Radiosondes Surface Maps: Regional
Landscape ( $\sim 1$ km)	Wet			3	0.75	0.2	Synop.	$R_n, G$ $H, LE$	$h$ $\theta, \delta\theta$ $q, \delta q$	Radiosondes Surface Maps: Landscape
	Dry			0.75	0.7	0.2	Synop.			
Local ( $\sim 10$ m)	Alfalfa			3	1.0	0.21	AWS	$R_n, G$ $H, LE$	$h$ $\theta, \delta\theta$ $q, \delta q$	Surface Fluxes
	Fallow			0.01	0.1	0.1	AWS			

## 5. Results

After developing the scaling scheme to integrate the observations in a conceptual modeling framework, and combining measurements to create a dataset to represent fluxes and advection across these scales, we can evaluate the results of the CLASS model runs across these scales. The results are presented with a bottom-up approach. In Section 5.1, we display the results for the surface energy components at all scales. In Section 5.2, we display the mixed-layer development at the regional and landscape scales.

### 5.1. Surface Energy Balance

#### *Observations*

To verify the results of the CLASS model, we focused on the surface energy budget components for each of the scales. We have observed surface fluxes at all scales via direct eddy-covariance at the local scales and the composite surface fluxes from the flux maps at the regional and landscape scales. At the local scale, we measured a  $\beta$  of  $\sim 30$  for the dry location and a  $\beta$  of  $\sim 0.01$  for the wet location. At larger scales, these extremes are tempered: we observed  $\beta$  of  $\sim 0.6$  and  $\sim 2.7$  for the wet and dry landscape scales respectively. At the regional scale, the observed Bowen ratios converged on a  $\beta$  of  $\sim 1.5$ . There were different surface fluxes depending on the spatial scale. We mimicked this in the CLASS model using parameter aggregation of the land surface based on the surface maps (Section 4.1).

#### *Regional and Landscape Scales*

At the regional scale, the net radiation was similar across the scales, however, the dry landscape had higher midday ground heat flux compared to the regional and the wet landscape scales (Fig. 6). This indicates that there is more available energy in the irrigated areas than the non-irrigated areas. ERA5 overestimated the ground heat flux at the regional scale, so it provided less available energy than there was in reality.

The partitioning of the available energy changed across the scales. In the wet landscape, approximately  $\frac{2}{3}$  of the available energy was contributing to latent heat flux compared to sensible heat flux. Conversely, in the dry landscape, approximately  $\frac{3}{4}$  of the available energy was partitioned into the sensible heat flux. At the regional scale, there was slightly more energy given to sensible heat flux than latent heat flux, but it fell somewhat in the middle of the wet and the dry landscapes. The model results for the latent heat flux match the observations reasonably for the wet landscape and regional scales; there was a slight dry bias in the regional scale model. Conversely, at the dry landscape scale, there was a dry bias in the latent heat flux, which corresponded to an overestimation of sensible heat flux at the same scale. This was likely due to the top layer of soil moisture that is prescribed to be drier than reality at this scale. The CLASS model overestimated the sensible heat flux relative to observations at all scales.

Compared to the CLASS model at the regional and landscape scales, ERA5 performs worst in all components of the surface energy balance. Although, the results of net radiation were reasonable, it overestimated ground heat flux, so ERA5 provided less available energy than observed. Moreover, ERA5 partitioned this energy almost entirely into the sensible heat flux.

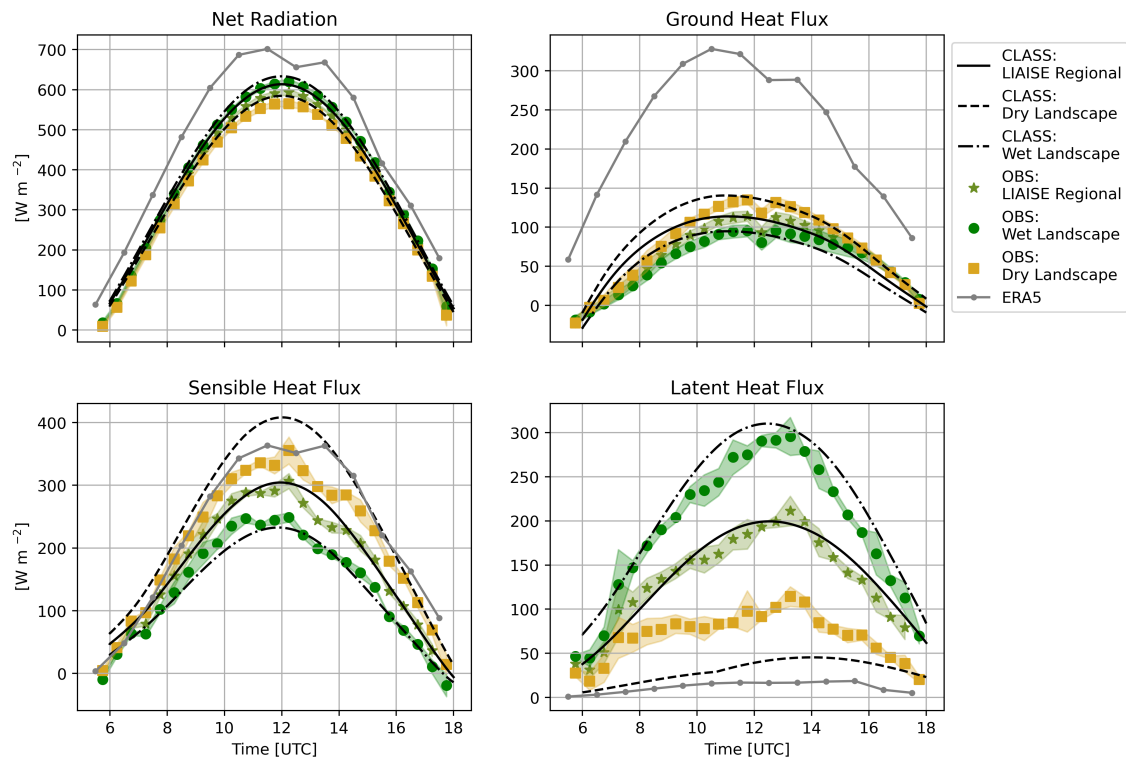


Figure 6: The components of the energy budget for the LIAISE composite day for both data (dots), CLASS model runs (black lines), and ERA5 (gray line). The data for the landscape (yellow and dark green) and regional scales (green-yellow) were calculated via the flux maps and the SEB network.

484 The sensible heat flux from ERA5 seems to be a reasonable match for the dry landscape scale,  
 485 however, ERA5 captured next to no latent heat flux in the LIAISE regional scale.

486 *Local Scales*

487 The local scales of the CLASS model were compared to the field level measurements in both  
 488 Els Plans and La Cendrosa (Fig. 7). The advection term described in Section 4.2 was prescribed  
 489 here for both the wet and fallow local scales respectively (black lines in Fig. 7). The brown  
 490 lines represent the local scale model case without advection applied for reference. At the local  
 491 scale, there was higher net radiation at the wet site than the dry site, which the CLASS model  
 492 was unable to capture. Between the higher outgoing longwave radiation and ground heat flux in  
 493 the dry site, overall, there was on average  $271 \text{ W m}^{-2} \text{ hr}^{-1}$  of additional energy at the irrigated  
 494 site compared to the dry site.

495 At the local scale, the surface fluxes were more extreme than at the landscape and regional  
 496 scales. The alfalfa local case had almost all of the energy partitioned into the latent heat flux.  
 497 At the alfalfa local scale, the sensible heat flux even became negative in the afternoon, which  
 498 the CLASS model was able to capture. Conversely, at the fallow local scale, all of the energy  
 499 was partitioned into the sensible heat flux, and there was little measured or modeled latent heat

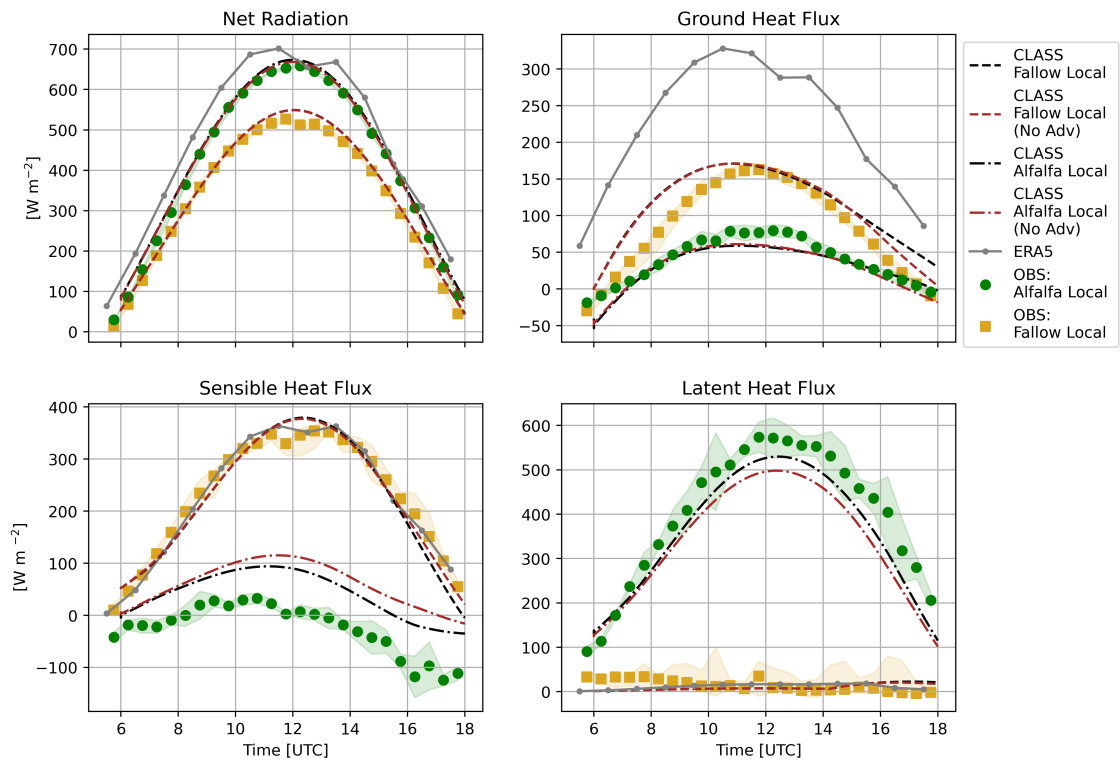


Figure 7: The components of the energy budget for the LIAISE composite day for both data (dots), CLASS model runs including advection (black lines), the CLASS model runs without advection (brown lines) and ERA5 (gray line). The observations and the CLASS model runs are only for the local scale.

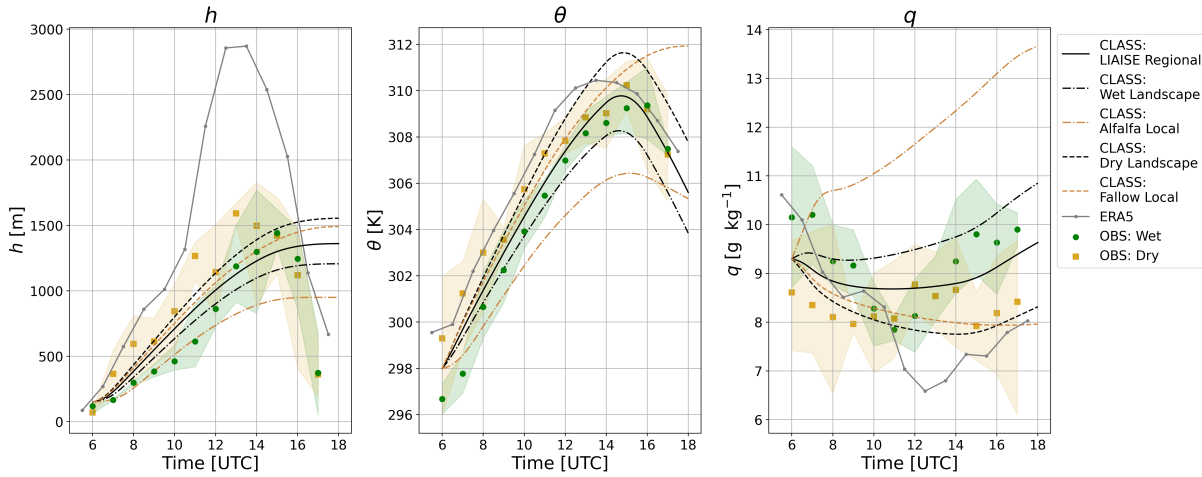


Figure 8: The components of the mixed layer for the LIAISE composite day for both data (dots), CLASS model runs for the landscape and regional scales (black lines) and the local scale (brown lines), and ERA5 (gray line) for the regional and landscape scales.

500 flux. The model case for the fallow local scale overestimated the sensible heat flux because  
 501 the extra available energy that the model prescribes is added to this term. Like the regional  
 502 and landscape cases, ERA5 overestimated the ground heat flux, however, it matched both the  
 503 sensible and latent heat flux for the fallow local scale better than any other scale.

504 *5.2. Mixed-Layer Development*

505 *Observations*

506 During the LIAISE composite day, the boundary layer grew to a maximum value of approxi-  
 507 mately 1500 m in both the wet and the dry areas (Fig. 8), but there is a clear difference in the  
 508 morning growth of the boundary layer. In the dry area, the boundary layer grew faster in the  
 509 early morning than in the wet area. This can be explained by the magnitude of the sensible heat  
 510 flux as shown in Figs. 7 and 8. It is evident from Fig. 8 that the maximum observed mixed-layer  
 511 height in the dry area is 150 m higher than the maximum in the wet area, but the timing of the  
 512 maximum boundary-layer height is different between landscapes. The mixed layer above the  
 513 dry area tended to be warmer and drier than the wet area. On average, the mixed layer in the  
 514 dry area was 1.3 K warmer and 0.87 g kg<sup>-1</sup> drier than the mixed layer in the wet area.

515 The maximum boundary-layer height occurred around 13:00 and 15:00 UTC for the wet and  
 516 dry sites respectively before the sea breeze arrived and stunted the boundary layer growth. The  
 517 temperature followed a similar pattern: the mixed layer heated up throughout the morning and  
 518 reached its maximum just before the sea breeze arrived in the late afternoon. In the morning,  
 519 the mixed layer was humid. As the boundary layer grew, it dried out for both the wet and the  
 520 dry areas. When the sea breeze arrived, the mixed layer humidified.

521 *Regional and Landscape Scales*



522 In Fig. 8 we show the results of the mixed-layer height and mean potential temperature and  
523 specific humidity for for the regional, landscape and local scales, ERA5 and the observations  
524 for the mixed layer over the LIAISE composite day. The modeled regional scale fell between  
525 the observed mixed layers in the wet and the dry areas. Although we do not have observations  
526 of the mixed layer for the regional scale, we assumed that the regional scale mixed-layer char-  
527 acteristics would fall somewhere between those measured in both the wet and dry areas as it  
528 is driven by the sensible and latent heat fluxes in the regional scale (Fig. 6). Therefore, the  
529 regional scale CLASS model captures the observed regional scale mixed layer. The landscape  
530 scale CLASS model cases demonstrated the differences observed in the wet and dry landscape;  
531 the wet landscape had a cooler and wetter mixed layer than the dry landscape.

532 ERA5 performed poorly for the boundary-layer height as it predicted a maximum boundary-  
533 layer height of 2870 m. This relates to its partitioning of the surface energy budget: nearly all of  
534 the available energy was prescribed to sensible heat flux, which was used to grow the boundary  
535 layer. This result can be replicated with the CLASS model when we switched off the interactive  
536 land surface model if the same  $\beta$  was prescribed. ERA5 captured the mixed-layer potential  
537 temperature well compared to the dry landscape observations, but it tended to dry out the mixed  
538 layer more than observed in either landscape.

## 539 **6. Discussion: Integration of Spatial Scales**

540 As shown in the previous section, the surface fluxes in a heterogeneous domain depend on  
541 the scale of the heterogeneity; however, we need to integrate processes across spatial scales  
542 to understand the processes that govern land-atmosphere interactions. Therefore, we will first  
543 discuss the limitations of our observational approach before exploring the feedbacks between  
544 surface fluxes and boundary-layer dynamics from our numerical experiments. Finally, we will  
545 discuss briefly the differences between ERA5 and our regional scale case.

546 We used observational data observed at the local scale to define the spatial scales in the  
547 CLASS model and to verify the dynamic behavior of the CLASS model. Nonetheless, some of  
548 the assumptions we made to create the flux maps warrant discussion. We assumed that surface  
549 characteristics, including  $LAI$  and the soil moisture can be linearly averaged over the domain.  
550 Some parameters - like soil composition and moisture - may be non-linear in space, so our  
551 procedure may cause errors in the observations that are used as model input. Another poten-  
552 tial limitation in the data approach is that there is a mismatch between what experimentalists  
553 measure with a single SEB station and how modelers use the data for model verification. Mea-  
554 surements are typically in the surface layer – well below the lowest grid cell of a model – and  
555 there could be problems with the constant flux layer assumption, as we observed in the alfalfa  
556 local scale. Furthermore, single point measurements have relatively small footprints compared  
557 to that of a model, so measurements are heavily impacted by surface conditions. It is unlikely  
558 that the a single SEB measurement is representative of all of that crop type in the LIAISE do-  
559 main. We addressed this mismatch in the data upscaling section (Section 4), but our method is  
560 limited through the assumption that all fields of a given crop type behave the same.

561 At the regional scale, we replicated surface fluxes using a composite of surface characteris-  
562 tics including soil moisture, vegetation cover and leaf area index. The observed regional scale  
563  $\beta$  was  $\sim 1.5$ , which was the necessary  $\beta$  to model the mixed-layer height using the conceptual  
564 model. At the local scales, microscale advection was required to correctly capture the high la-  
565 tent heat fluxes in the alfalfa local scale. At this scale, the sensible heat flux became negative in  
566 the afternoon, which we were able to capture with the CLASS model. We also found that this  
567 negative heat flux only occurs locally. It has been observed only in the roughness sublayer of the  
568 La Cendrosa alfalfa field. This suggests that non-local processes are impacting the local scale,  
569 including advection. Because this is such a local phenomenon, it implies there is an internal  
570 boundary layer that forms in the heaviest vegetative areas within the wet landscape scale. This  
571 could mean that energy from the regional or landscape scales impact the local energy budget.

572 At the landscape scales, the surface fluxes were less extreme than local scales; however,  
573 they retained more of the characteristics of the different surfaces than the regional scale. This  
574 is because the landscape scales are not entirely wet or dry: there was a mix of crop types across  
575 both scales. For example, fluxes from fruit and nut trees – both with and without irrigation –  
576 have higher  $\beta$  than the annual crops like maize or alfalfa. For that reason, the crop mixture  
577 moderates the fluxes in both the wet and the dry landscapes. In the wet landscape scale, there  
578 are drier fields and even fallow fields which drove the boundary layer development.

579 Because the sensible heat flux is one of the most important factors in determining boundary-  
580 layer height (Ball, 1960), the mixed layer results for each scale changed based on the surface  
581 fluxes. We found that a modeled  $\beta$  of  $\sim 1.8$  replicates the correct mixed-layer characteristics  
582 defined by the boundary layer growth and the diurnal variability of state variables. This is just  
583 slightly higher than what we measured at the regional scale, which implies that the boundary  
584 layer on the regional scale is formed via a composite of surface fluxes from the LIAISE region.  
585 This is supported by the fact that the mean of the surface fluxes for wet and dry landscape  
586 cases is approximately the surface fluxes from the regional scale. The regional scale had a  
587 boundary-layer height that is 10% higher and 8% lower than the wet and dry landscape scales  
588 respectively. Therefore, even at the landscape scale, a composite of surface characteristics is  
589 able to reproduce the growth of the boundary layer.

590 We did not capture the sea breeze well at the end of the model period, which is due to the  
591 assumption of no synoptic scale subsidence. In the CLASS model, the boundary layer can only  
592 shrink if (1) the sensible heat flux is negative or (2) there is a contribution of the large-scale  
593 subsidence. When the sea breeze arrived, the observed sensible heat flux at the regional scale  
594 was positive, so even including advection, we could not capture the collapse of the mixed-layer  
595 height without imposing subsidence. One should be aware of the sea breeze when interpreting  
596 the mixed-layer results at the end of the afternoon.

597 At the local scale, surface fluxes were more extreme; however, we found that the fallow local  
598 case also well represents the boundary-layer height and temperature. The wet landscape case  
599 showed a marked difference in boundary-layer height (30% lower), temperature (2 K cooler),  
600 and specific humidity ( $0.3 \text{ g kg}^{-1}$  wetter) than the regional case. This illustrates that the regional  
601 scale boundary layer is more influenced by the presence of the extremely dry fields than those

602 of the extremely wet fields. Furthermore, because we added advection in the local cases and  
603 the mixed layer for the alfalfa local scale does not match that of the regional scale, we can infer  
604 that the mixed layer – even at the local scales – is formed by a composite of surface fluxes in  
605 the region instead of the boundary layer being advected from downwind. This could mean that  
606 if the dry region were to be irrigated in the future, there would be a pronounced difference in  
607 the regional boundary layer compared to now.

608 The idea that there is an internal boundary layer over the wet region and that the regional  
609 boundary layer is formed by a composite of surface fluxes was supported by the radiosonde  
610 observations in Fig. 2. The radiosonde over La Cendrosa, which was characterized by stable  
611 thermal stratification, gradually dries and warms with height as it began to observe fluxes that  
612 originate from the regional scale. Moreover, the radiosonde from Els Plans observed a mixed  
613 layer that is both cooler and wetter than its surface. With this analysis, it is not apparent if there  
614 is a traditional internal boundary layer that is formed on the local and landscape scales, or if it  
615 better matches the idea of a blending height where the regional measurements converge within  
616 the boundary layer.

617 At the local scale when we added advection (Fig. 7), we could quantify how much the non-  
618 local boundary-layer processes impact the surface fluxes in both the alfalfa and fallow fields.  
619 With advection in the alfalfa local scale, the latent heat flux was 10% higher and the sensible  
620 heat flux was 13% lower than the case without advection. The mean differences do not tell  
621 the entire story: the inclusion of advection allows the slight temporal shift in the latent heat  
622 flux compared to net radiation observed in Figs. 2 and 7. It also ensures that the sensible  
623 heat flux becomes negative in the afternoon locally. At the fallow local scale, the inclusion of  
624 advection did not appreciably change the latent heat flux; however, it changed how quickly the  
625 surface cools down during the sea breeze, which impacted the partitioning between sensible and  
626 ground heat flux in the late afternoon.

627 Mixed-layer theory has no applicability during times of stable stratification, which has been  
628 observed in the afternoon at the alfalfa local scale. However, because the stably stratified air  
629 near the surface is topped by a convective boundary layer, we apply the CLASS model to capture  
630 the convective layer above it. For that reason, we cannot capture the correct sensible heat flux  
631 nor the correct boundary layer stratification at this scale without the presence of advection. At  
632 the alfalfa local scale, the main limitation of applying a mixed-layer model is that one is unable  
633 to capture the internal boundary layer that was observed.

634 In order to understand why ERA5 performed badly in the LIAISE domain, we should con-  
635 sider that by using the CLASS model, we replicated a land surface model that prescribes het-  
636 erogeneous surfaces using the parameter aggregation method, while ERA5 uses the flux aggre-  
637 gation approach. We found that ERA5 best matches the local surface fluxes from Els Plans  
638 (fallow local scale), although its spatial extent was that of the regional scale. We hypothesize  
639 that the reason ERA5 performs badly in the domain is that it fails to capture the subgrid scale  
640 heterogeneity due to irrigation. The average soil moisture across all tiles is  $0.1 \text{ m m}^{-3}$ , which  
641 is similar to that measured in the top 5 cm of Els Plans. The lack of soil moisture insures  
642 that even if the vegetation were to be parameterized correctly, there is not enough water in the

643 model to correctly partition the surface fluxes. Capturing irrigation (or the lack thereof) is a  
644 well-documented weakness in weather and climate models in arid and semi-arid agricultural ar-  
645 eas (Alexander et al., 2022; Lawston et al., 2015, 2020; Qian et al., 2020). However, we found  
646 that the lack of irrigation is a small part of the differences between ERA5 and our regional scale  
647 case. When we ran the regional case using the soil moisture from ERA5, we found that the  $\beta$   
648 increases from  $\sim 1.8$  to  $\sim 2.2$  (compared with  $\beta_{ERA5} \sim 17.9$ ). The difference in the mixed-layer  
649 characteristics is negligible between the regional case and the regional case run with ERA5 soil  
650 moisture. Instead, the difference in the boundary-layer development must be explained through  
651 a combination of the vegetation characteristics and the available soil moisture.

## 652 7. Summary and Conclusions

653 In this study, we introduced a site-specific framework to investigate how observations of  
654 the boundary-layer dynamics connect to the surface energy budget across spatial scales. We  
655 used comprehensive observations of surface and atmospheric observations from the two-week  
656 LIAISE campaign in July 2021. The LIAISE domain was characterized by an extreme surface  
657 heterogeneity; there was a sharp contrast between an irrigation area ( $\sim 10$  km) and the semi-  
658 arid area. The LIAISE experiment offered a unique possibility to study both how the surface  
659 heterogeneity controls on the boundary-layer dynamics and how the boundary-layer dynamics  
660 controls the diurnal variability of surface fluxes across spatial scales. We interpreted the scal-  
661 ing scheme by using a conceptual mixed-layer land-atmosphere model coupled to various land  
662 surfaces characterized by extreme heterogeneity. This study offered a unique opportunity to  
663 determine the reliability of land surface models in a heterogeneous environment. The intro-  
664 duced framework for interpolating spatial scales of heterogeneity is a promising method for  
665 verifying the performance of land surface models in heterogeneous areas.

666 By combining observations and systematic numerical results, we were able to quantify the  
667 relationship between surface properties and boundary-layer dynamics at local ( $\sim 100$  m), land-  
668 scape ( $\sim 1$  km) and regional ( $\sim 10$  km) scales. Our aim was to connect the “large-patch” type of  
669 heterogeneity from the regional scale with the “unstructured” type of heterogeneity at the land-  
670 scape scales and the “statistically homogeneous microscale” heterogeneity at the local scales.  
671 We raised two research questions to disentangle the bidirectional impacts between the land  
672 surface and the boundary-layer dynamics specifically for the LIAISE domain.

673 1. *How does a heterogeneous surface control the boundary-layer dynamics across spatial*  
674 *scales?*

675 The observed  $\beta$  in the alfalfa (wet) field was  $\sim 0.01$  while the observed  $\beta$  in the fallow (dry)  
676 field was  $\sim 30$ , but the observed evolution of boundary-layer characteristics were similar despite  
677 the extreme surfaces. Using a land-atmosphere coupled model, we found that a  $\beta$  of  $\sim 1.8$   
678 was required to form the observed boundary-layer characteristics. This was slightly higher  
679 than the observed  $\beta$  at the regional scale ( $\beta \sim 1.5$ ) at the LIAISE regional scale. Using the  
680 observed surface fluxes, where the local surface fluxes are more extreme, the modeled mixed

681 layer differed from the observed boundary-layer growth. The local fallow scale mean boundary-  
682 layer height was 10% higher than the regional scale and the local alfalfa scale mean boundary-  
683 layer height was 34% lower than the regional scale . This indicates that the observed boundary  
684 layer is formed from the aggregated regional landscape where the dry landscape has slightly  
685 more weight than the wet landscape, and there was an internal boundary layer that forms in the  
686 wet landscape and local scales. Therefore, advection was necessary to describe the boundary  
687 layer at local scales.

688 *2. What is the impact of the boundary-layer dynamics on the diurnal variability of the sur-*  
689 *face fluxes?*

690 In analyzing the influence of boundary-layer dynamics on surface fluxes, we found that another  
691 non-local effect plays a key role in reproducing the observations with the model: the advection  
692 of heat and moisture. We determined advection by calculating gradients of temperature and  
693 moisture from an AWS network in the LIAISE domain. During the day, there was warm,  
694 dry air advection within the wet landscape and cool, moist air advection across the wet-dry  
695 boundary. In the late afternoon after the sea breeze arrives, both the irrigated and dry landscapes  
696 experienced cool and moist advection. At the local scale, the inclusion of advection of heat  
697 and moisture was important for capturing the both the magnitude and timing diurnal cycle of  
698 surface fluxes. In the alfalfa (wet) local scale, advection allowed for more latent heat flux than  
699 the surface alone would allow, especially in the afternoon. At the landscape and regional scales,  
700 it appears that the boundary-layer dynamics played a less important role than the surface in  
701 controlling the partitioning of energy at the surface.

702 By using a coupled land-atmosphere model constrained by observations, we could disentangle  
703 the controls that the boundary layer exerts on the surface and those that the surface exerts  
704 on the boundary-layer dynamics. In thermally heterogeneous environments, land-atmosphere  
705 interactions are complex: there are non-local drivers of both the atmospheric boundary layer  
706 and the partitioning of energy. We introduced a site-specific scaling framework to address the  
707 role that spatial scale plays in a subgrid scale heterogeneity, which can offer a template for  
708 future studies. We find that local scale surface observations are insufficient for explaining the  
709 boundary-layer dynamics at any scale. Instead, the observed boundary layer is formed via com-  
710 posite fluxes of sensible and latent heat over a horizontal extent of 10 km. In the LIAISE region,  
711 which is characterized by strong thermal heterogeneity, we found that the regional surface prop-  
712 erties developed the boundary-layer dynamics, but the boundary layer feedback on the heat and  
713 moisture surface fluxes was a much less clear connection. In the future, this framework for  
714 surface heterogeneity can be used to evaluate the drivers of latent heat flux to further investigate  
715 the impacts of the boundary-layer dynamics on the surface fluxes.

## 716 **Acknowledgements**

717 We would like to thank all of organizers, hosts and participants of the LIAISE campaign.  
718 In particular, we would like to acknowledge Martin Best, Joaquim Bellvert, Jennifer Brooke,

719 Jan Polcher and Pere Quintana for their work on the LIAISE steering committee, and Henk  
720 Snellen, Getachew Adnew, Marc Castellnou, Jerry Chen, Kevin van Diepen, Kim Faassen,  
721 Raquel Gonzalez Armas, Wouter Mol, Robbert Moonen, Ruben Schulte and Gijs Vis for their  
722 work on the LIAISE-NL team during the experiment. Pere Quintana also provided the crop  
723 cover maps in the Ebro River Valley.

724 We would like to thank the two anonymous reviewers for their comments which greatly im-  
725 proved the quality of this paper.

726 This PhD project partly was supported by the appointment of Jordi Vila as Chair of the Meteo-  
727 rology and Air Quality Group of Wageningen University.

## 728 **Appendix A**

729 The SIGPAC land use map was reclassified to match the measured land cover types in the  
730 LIAISE domain (Fig. 9 and Table 3). Table 3 shows the original crop types and how they  
731 were reclassified to match the LIAISE experiment, while Fig. 9 shows the reclassified land use  
732 map that has been used to make the flux maps. There were a number of assumptions made to  
733 reclassify the actual crop types into the LIAISE land use types:

- 734 • **Cereal** In the LIAISE region, there are multiple types of cereal crops grown during the  
735 winter in the rainfed area including wheat, barley and oats. We assumed that by July, all  
736 of these cereal crops had been harvested, so that a fallow field or one with dry stubble  
737 remained. Therefore, we use the measurements from Els Plans to represent all cereal  
738 crops.
- 739 • **Maize** In the irrigated region, corn accounted for 20% of the landscape (Table 3). There  
740 were two stations measuring in corn fields during the LIAISE campaign, so these sites  
741 were averaged together to provide a more robust measure of the variability of maize fields  
742 in the region during the LIAISE campaign. We assumed with maize, most fields were in  
743 approximately the same growth stage and that they were all pre-senescent.
- 744 • **Alfalfa** In the irrigated area, alfalfa accounted for approximately 15% of the landscape  
745 (Table 3). The LIAISE campaign fell within one growing cycle of alfalfa: the campaign  
746 began about a week after harvest and five days after the first irrigation. Therefore, we  
747 measured one alfalfa growing cycle from nearly bare soil to full crop cover. In order to  
748 properly replicate the temporal variability of growing stage in the regional alfalfa, we  
749 apply a growing stage to each alfalfa pixel and use the observed surface fluxes from  
750 the La Cendrosa alfalfa field at that stage. Because the surface plays an important role in  
751 determining both the available energy and its partitioning, we take all surface components  
752 instead of recalculating fluxes based on a Bowen ratio. This means that we have to assume  
753 that daily variability in synoptic and boundary layer dynamics are constant throughout the  
754 LIAISE domain, which is not necessarily true.

Table 3: Reclassification scheme from SIGPAC crop cover to match the measurements of LIAISE SEB stations. The re-classified crop type is the selected land cover that matches a surface energy budget (SEB) station. The left three columns display the proportion of the total land cover that each crop type makes up across the regional and landscape scales.

Re-classified Crop	SEB Station	SIGPAC Crop	% Regional	% Wet Landscape	% Dry Landscape
Cereals	Els Plans – Natural Vegetation	Soft Wheat, Colza, Barley, Oat, Triticale, Vetch, Peas	36.1	22.7	50.0
Maize	Boldu Maize and IRTA Maize	Corn	12.5	20.0	4.4
Alfalfa	La Cendrosa – Alfalfa	Alfalfa	8.5	14.6	2.0
Grass	IRTA – Grass	Festuca Grass, Ray-Grass	2.7	4.4	0.7
Vineyards	Verdu – Vineyard	Vineyards	1.0	0.1	2.0
Fruit Trees	IRTA – Apple	Olive, Pear, Peach, Nectarine, Apricot, Date, Apple, Other Fruit Trees	13.3	16.0	10.3
Nut Trees	Prexiana – Almonds	Almond Trees	1.7	0.7	3.0
Urban	Modeled	N/A	21.2	19.6	23.3
Water	Modeled	N/A	0.27	0.5	0.0

- 755 • **Fruit Orchards** We assume that the energy partitioning between different types of fruit  
756 trees (e.g. apple, pear, olives) are similar. There are also fruit trees located in both the  
757 irrigated and rainfed areas, but our reference apple orchard is partially irrigated; however,  
758 there were weighing lysimeter in both irrigated and non-irrigated apple trees in the or-  
759 chard which were used to correct the Bowen ratio of the eddy-covariance system for the  
760 non-irrigated area.
- 761 • **Nut Orchards** We measured in one non-irrigated almond orchard during the LIAISE  
762 campaign. Because most of the almonds were all located in the non-irrigated area, it is  
763 fair to assume that all almond trees behave similarly.
- 764 • **Vineyards** Like almond orchards, most of the vineyards were located in the non-irrigated  
765 area where where the vineyard surface energy budget (SEB) station was located. Like the  
766 almond trees, the one station is likely representative of all of the vineyards.
- 767 • **Water** There is a lake in the irrigated region. In this study, we modeled the energy budget  
768 for the water. In the future, energy budget components measured directly from the lake  
769 will be available. The flux maps will be updated to reflect this.

770 In addition to creating surface flux maps, we have also created products using the leaf-level  
771 ecological measurements including leaf area index, vegetative fraction, stomatal conductance,  
772 surface resistance, and soil respiration. Although these products are not shown, they were used  
773 to create the composite land surface at different scales used in the CLASS model. In the future,  
774 we hope to maps for net ecosystem exchange, soil moisture and temperature from the data

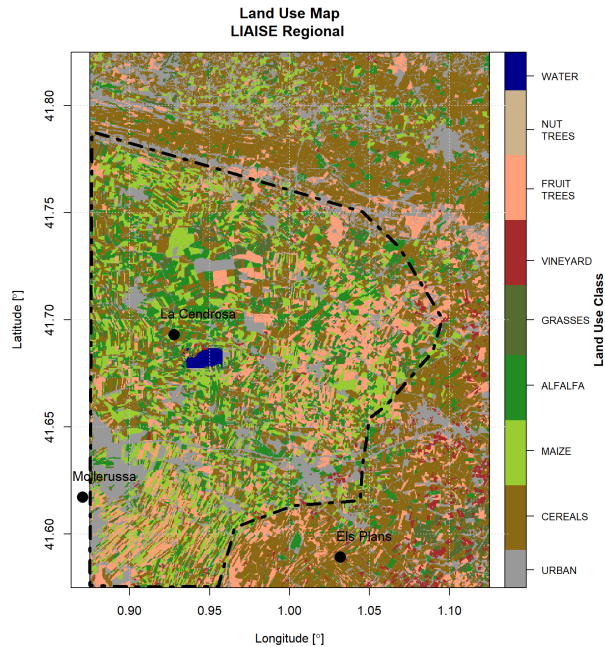


Figure 9: The reclassified 100 m SIGPAC crop cover map for the LIAISE regional scale.

775 collected in the LIAISE network of SEB stations. The data from the LIAISE Unified Eddy-  
 776 Covariance processing as well as the flux maps will be available to the LIAISE community and  
 777 the public through the LIAISE database (<https://liaise.aeris-data.fr/>).

## 778 Appendix B

779 We must make a number of assumptions in order to use the network of AWS locations to  
 780 calculate boundary-layer advection:

- 781 1. We calculate advection with 2 m temperature and humidity and 10 m wind velocity to  
 782 represent of the boundary-layer advection. This assumption will induce errors in our  
 783 advection estimates because 2 m observations are heavily influenced by the surface con-  
 784 ditions.
- 785 2. For the alfalfa local scale, we assume that the advection is the average of the advection  
 786 across the wet landscape. Therefore, we have selected AWS stations in the irrigated part  
 787 of the LIAISE domain to calculate advection (blue and white locations Fig. 5a).
- 788 3. For the fallow local scale, we assume that the advection is that which crosses from the wet  
 789 landscape into the dry landscape. Therefore, we have selected AWS near the boundary of  
 790 the wet-dry boundary (white and red locations in Fig. 5a).
- 791 4. We assume that the 10 m wind speed and direction is constant on the landscape scale.



792 5. The stations for each scale are aligned by mean wind direction for a 10-minute interval.  
793 The advection term is calculated using

$$adv_x = \bar{U} \frac{dX}{dr} \quad (3)$$

794 where  $\bar{U}$  is the mean wind speed,  $\frac{dX}{dr}$  is the gradient of the scalar (e.g. potential temper-  
795 ature or specific humidity) between stations that align in the mean wind direction where  
796  $dr$  is the distance between stations.

797 6. Stations that fall within a 30° window from the mean wind direction of another station are  
798 used to calculate the gradient of the scalar. All combinations of stations that fall within  
799 the 30° window of the mean wind direction are averaged together to find the advection  
800 for a 10 minute interval.

801 7. The advection term is calculated from a mean of all scalar gradients from all appropriate  
802 station combinations for a given wind direction.

## References

- Alexander, G.A., Holmes, H.A., Sun, X., Caputi, D., Faloona, I.C., Oldroyd, H.J., 2022. Simulating land-atmosphere coupling in the Central Valley, California: Investigating soil moisture impacts on boundary layer properties. *Agricultural and Forest Meteorology* 317, 108898. doi:10.1016/j.agrformet.2022.108898.
- Vilà-Guerau de Arellano, J., van Heerwaarden, C.C., van Stratum, B.J.H., van den Dries, K., 2015. *Atmospheric Boundary Layer: Integrating Chemistry and Land Interactions*. Cambridge University Press, New York, New York.
- Vilà-Guerau de Arellano, J., Ney, P., Hartogensis, O., de Boer, H., van Diepen, K., Emin, D., de Groot, G., Klosterhalfen, A., Langensiepen, M., Matveeva, M., Miranda-García, G., Moene, A.F., Rascher, U., Röckmann, T., Adnew, G., Brüggemann, N., Rothfuss, Y., Graf, A., 2020. CloudRoots: integration of advanced instrumental techniques and process modelling of sub-hourly and sub-kilometre land-atmosphere interactions. *Biogeosciences* 17, 4375–4404. doi:10.5194/bg-17-4375-2020.
- Baldocchi, D., Falge, E., Gu, L., Olson, R., Hollinger, D., Running, S., Anthoni, P., Bernhofer, C., Davis, K., Evans, R., Fuentes, J., Goldstein, A., Katul, G., Law, B., Lee, X., Malhi, Y., Meyers, T., Munger, W., Oechel, W., U, K.T.P., Pilegaard, K., Schmid, H.P., Valentini, R., Verma, S., Vesala, T., Wilson, K., Wofsy, S., 2001. FLUXNET: A New Tool to Study the Temporal and Spatial Variability of Ecosystem-Scale Carbon Dioxide, Water Vapor, and Energy Flux Densities. *Bulletin of the American Meteorological Society* 82, 2415–2434. doi:10.1175/1520-0477(2001)082<2415:FANTTS>2.3.CO;2.

- Baldocchi, D.D., Hincks, B.B., Meyers, T.P., 1988. Measuring Biosphere-Atmosphere Exchanges of Biologically Related Gases with Micrometeorological Methods. *Ecology* 69, 1331–1340. doi:10.2307/1941631.
- Ball, F.K., 1960. Control of inversion height by surface heating. *Q.J Royal Met. Soc.* 86, 483–494. doi:10.1002/qj.49708637005.
- Beamesderfer, E.R., Buechner, C., Faiola, C., Helbig, M., Sanchez-Mejia, Z.M., Yáñez-Serrano, A.M., Zhang, Y., Richardson, A.D., 2022. Advancing Cross-Disciplinary Understanding of Land-Atmosphere Interactions. *Journal of Geophysical Research: Biogeosciences* 127, e2021JG006707. doi:10.1029/2021JG006707.
- Boone, A., Bellvert, J., Best, M., Brooke, J., Canut-Rocafort, G., Cuxart, J., Hartogensis, O., e Moigne, P., Miró, J.R., Polcher, J., Price, J., Quintana Seguí, P., Wooster, M., 2021. Updates on the International Land Surface Interactions with the Atmosphere over the Iberian Semi-Arid Environment (LIAISE) Field Campaign. *GEWEX News* 31, 17–21.
- Boone, A., Best, M., Cuxart, J., Polcher, J., Quintana, P., Bellvert, J., Brooke, J., Canut-Rocafort, G., Price, J., 2019. Land Surface Interactions with the Atmosphere over the Iberian Semi-Arid Environment (LIAISE). *GEWEX News* 29, 8–10.
- Bou-Zeid, E., Anderson, W., Katul, G.G., Mahrt, L., 2020. The Persistent Challenge of Surface Heterogeneity in Boundary-Layer Meteorology: A Review. *Boundary-Layer Meteorol* 177, 227–245. doi:10.1007/s10546-020-00551-8.
- Bou-Zeid, E., Meneveau, C., Parlange, M.B., 2004. Large-eddy simulation of neutral atmospheric boundary layer flow over heterogeneous surfaces: Blending height and effective surface roughness. *Water Resources Research* 40. doi:10.1029/2003WR002475.
- Butterworth, B.J., Desai, A.R., Townsend, P.A., Petty, G.W., Andresen, C.G., Bertram, T.H., Kruger, E.L., Mineau, J.K., Olson, E.R., Paleri, S., Pertzborn, R.A., Pettersen, C., Stoy, P.C., Thom, J.E., Vermeuel, M.P., Wagner, T.J., Wright, D.B., Zheng, T., Metzger, S., Schwartz, M.D., Iglinski, T.J., Mauder, M., Speidel, J., Vogelmann, H., Wanner, L., Augustine, T.J., Brown, W.O.J., Oncley, S.P., Buban, M., Lee, T.R., Cleary, P., Durden, D.J., Florian, C.R., Lantz, K., Riihimaki, L.D., Sedlar, J., Meyers, T.P., Plummer, D.M., Guzman, E.R., Smith, E.N., Sühring, M., Turner, D.D., Wang, Z., White, L.D., Wilczak, J.M., 2021. Connecting Land–Atmosphere Interactions to Surface Heterogeneity in CHEESEHEAD19. *Bulletin of the American Meteorological Society* 102, E421–E445. doi:10.1175/BAMS-D-19-0346.1.
- Buttner, G., 2014. CORINE Land Cover and Land Cover Change Products, in: Manakos, I., Braun, M. (Eds.), *Land Use and Land Cover Mapping in Europe: Practices & Trends*. Springer, Dordrecht, the Netherlands, pp. 55–74.

- Conzemius, R., Fedorovich, E., 2007. Bulk Models of the Sheared Convective Boundary Layer: Evaluation through Large Eddy Simulations. *Journal of the Atmospheric Sciences* 64, 786–807. doi:10.1175/JAS3870.1.
- Driedonks, A.G.M., Tennekes, H., 1984. Entrainment effects in the well-mixed atmospheric boundary layer. *Boundary-Layer Meteorol* 30, 75–105. doi:10.1007/BF00121950.
- Fratini, G., Mauder, M., 2014. Towards a consistent eddy-covariance processing: an inter-comparison of EddyPro and TK3. *Atmospheric Measurement Techniques* 7, 2273–2281. doi:10.5194/amt-7-2273-2014.
- Grimmond, C.S.B., Oke, T.R., 1999. Aerodynamic Properties of Urban Areas Derived from Analysis of Surface Form. *Journal of Applied Meteorology and Climatology* 38, 1262–1292. doi:10.1175/1520-0450(1999)038<1262:APOUAD>2.0.CO;2.
- van Heerwaarden, C.C., Vilà-Guerau de Arellano, J., Moene, A.F., Holtslag, A.A.M., 2009. Interactions between dry-air entrainment, surface evaporation and convective boundary-layer development. *Quarterly Journal of the Royal Meteorological Society* 135, 1277–1291. doi:10.1002/qj.431.
- van Heerwaarden, C.C., Mellado, J.P., Lozar, A.D., 2014. Scaling Laws for the Heterogeneously Heated Free Convective Boundary Layer. *Journal of Atmospheric Sciences* 71, 3975–4000. doi:10.1175/JAS-D-13-0383.1.
- Helbig, M., Gerken, T., Beamesderfer, E.R., Baldocchi, D.D., Banerjee, T., Biraud, S.C., Brown, W.O.J., Brunsell, N.A., Burakowski, E.A., Burns, S.P., Butterworth, B.J., Chan, W.S., Davis, K.J., Desai, A.R., Fuentes, J.D., Hollinger, D.Y., Kljun, N., Mauder, M., Novick, K.A., Perkins, J.M., Rahn, D.A., Rey-Sanchez, C., Santanello, J.A., Scott, R.L., Seyednasrollah, B., Stoy, P.C., Sullivan, R.C., de Arellano, J.V.G., Wharton, S., Yi, C., Richardson, A.D., 2021. Integrating continuous atmospheric boundary layer and tower-based flux measurements to advance understanding of land-atmosphere interactions. *Agricultural and Forest Meteorology* 307, 108509. doi:10.1016/j.agrformet.2021.108509.
- Hersbach, H., Bell, B., Berrisford, P., Hirahara, S., Horányi, A., Muñoz-Sabater, J., Nicolas, J., Peubey, C., Radu, R., Schepers, D., Simmons, A., Soci, C., Abdalla, S., Abellan, X., Balsamo, G., Bechtold, P., Biavati, G., Bidlot, J., Bonavita, M., De Chiara, G., Dahlgren, P., Dee, D., Diamantakis, M., Dragani, R., Flemming, J., Forbes, R., Fuentes, M., Geer, A., Haimberger, L., Healy, S., Hogan, R.J., Hólm, E., Janisková, M., Keeley, S., Laloyaux, P., Lopez, P., Lupu, C., Radnoti, G., de Rosnay, P., Rozum, I., Vamborg, F., Villaume, S., Thépaut, J.N., 2020. The ERA5 global reanalysis. *Quarterly Journal of the Royal Meteorological Society* 146, 1999–2049. doi:10.1002/qj.3803.
- Institut Cartogràfic i Geològic de Catalunya, 2009-2020. Gt iv. soil map 1:25,000. URL: <https://www.icgc.cat/en/Public-Administration-and-Enterprises/>

Downloads/Geological-and-geothematic-cartography/Soil-cartography/GT-IV.-Soil-map-1-25-000.

- Kadyrov, N., Broquet, G., Chevallier, F., Rivier, L., Gerbig, C., Ciais, P., 2015. On the potential of the ICOS atmospheric CO<sub>2</sub> measurement network for estimating the biogenic CO<sub>2</sub> budget of Europe. *Atmospheric Chemistry and Physics* 15, 12765–12787. doi:10.5194/acp-15-12765-2015.
- Kaimal, J.C., Finnigan, J.J., 1994. *Atmospheric boundary layer flows: their structure and measurement*. Oxford University Press, New York.
- Lawston, P.M., Santanello, J.A., Hanson, B., Arsensault, K., 2020. Impacts of Irrigation on Summertime Temperatures in the Pacific Northwest. *Earth Interactions* 24, 1–26. doi:10.1175/EI-D-19-0015.1.
- Lawston, P.M., Santanello, J.A., Zaitchik, B.F., Rodell, M., 2015. Impact of Irrigation Methods on Land Surface Model Spinup and Initialization of WRF Forecasts. *Journal of Hydrometeorology* 16, 1135–1154. doi:10.1175/JHM-D-14-0203.1.
- Lemonsu, A., Grimmond, C.S.B., Masson, V., 2004. Modeling the Surface Energy Balance of the Core of an Old Mediterranean City: Marseille. *Journal of Applied Meteorology (1988-2005)* 43, 312–327.
- Lothon, M., Lohou, F., Pino, D., Couvreux, F., Pardyjak, E.R., Reuder, J., Vilà-Guerau de Arellano, J., Durand, P., Hartogensis, O., Legain, D., Augustin, P., Gioli, B., Lenschow, D.H., Faloua, I., Yagüe, C., Alexander, D.C., Angevine, W.M., Bargain, E., Barrié, J., Bazile, E., Bezombes, Y., Blay-Carreras, E., van de Boer, A., Boichard, J.L., Bourdon, A., Butet, A., Campistron, B., de Coster, O., Cuxart, J., Dabas, A., Darbieu, C., Deboudt, K., Delbarre, H., Derrien, S., Flament, P., Fourmentin, M., Garai, A., Gibert, F., Graf, A., Groebner, J., Guichard, F., Jiménez, M.A., Jonassen, M., van den Kroonenberg, A., Magliulo, V., Martin, S., Martinez, D., Mastrorillo, L., Moene, A.F., Molinos, F., Moulin, E., Pietersen, H.P., Pignatelli, B., Pique, E., Román-Cascón, C., Rufin-Soler, C., Saïd, F., Sastre-Marugán, M., Seity, Y., Steeneveld, G.J., Toscano, P., Traullé, O., Tzanos, D., Wacker, S., Wildmann, N., Zaldei, A., 2014. The BLLAST field experiment: Boundary-Layer Late Afternoon and Sunset Turbulence. *Atmospheric Chemistry and Physics* 14, 10931–10960. doi:https://doi.org/10.5194/acp-14-10931-2014.
- Noilhan, J., Mahfouf, J.F., 1996. The ISBA land surface parameterisation scheme. *Global and Planetary Change* 13, 145–159. doi:10.1016/0921-8181(95)00043-7.
- Noilhan, J., Planton, S., 1989. A Simple Parameterization of Land Surface Processes for Meteorological Models. *Monthly Weather Review* 117, 536–549. doi:10.1175/1520-0493(1989)117<0536:ASPOLS>2.0.CO;2.

- Patton, E.G., Sullivan, P.P., Moeng, C.H., 2005. The Influence of Idealized Heterogeneity on Wet and Dry Planetary Boundary Layers Coupled to the Land Surface. *J. Atmos. Sci.* 62, 2078–2097. doi:10.1175/JAS3465.1.
- Qian, Y., Yang, Z., Feng, Z., Liu, Y., Gustafson, W.I., Berg, L.K., Huang, M., Yang, B., Ma, H.Y., 2020. Neglecting irrigation contributes to the simulated summertime warm-and-dry bias in the central United States. *npj Clim Atmos Sci* 3, 1–10. doi:10.1038/s41612-020-00135-w.
- Raasch, S., Harbusch, G., 2001. An Analysis Of Secondary Circulations And Their Effects Caused By Small-Scale Surface Inhomogeneities Using Large-Eddy Simulation. *Boundary-Layer Meteorology* 101, 31–59. doi:10.1023/A:1019297504109.
- Román-Cascón, C., Lothon, M., Lohou, F., Hartogensis, O., Vila-Guerau de Arellano, J., Pino, D., Yagüe, C., Pardyjak, E.R., 2021. Surface representation impacts on turbulent heat fluxes in WRF(v4.1.3). preprint. *Atmospheric sciences*. doi:10.5194/gmd-2020-371.
- Shen, S., Leclerc, M.Y., 1994. Large-eddy simulation of small-scale surface effects on the convective boundary-layer structure. *Atmosphere-Ocean* 32, 717–731. doi:10.1080/07055900.1994.9649519.
- Shen, S., Leclerc, M.Y., 1995. How large must surface inhomogeneities be before they influence the convective boundary layer structure? A case study. *Quarterly Journal of the Royal Meteorological Society* 121, 1209–1228. doi:https://doi.org/10.1002/qj.49712152603.
- Swinbank, W.C., 1951. The Measurement of Vertical Transfer of Heat and Water Vapor by Eddies in the lower Atmosphere. *Journal of the Atmospheric Sciences* 8, 135–145. doi:10.1175/1520-0469(1951)008<0135:TMOVTO>2.0.CO;2.
- Tennekes, H., 1973. A Model for the Dynamics of the Inversion Above a Convective Boundary Layer. *Journal of the Atmospheric Sciences* 30, 558–567. doi:10.1175/1520-0469(1973)030<0558:AMFTDO>2.0.CO;2.
- Twine, T.E., Kustas, W.P., Norman, J.M., Cook, D.R., Houser, P.R., Meyers, T.P., Prueger, J.H., Starks, P.J., Wesely, M.L., 2000. Correcting eddy-covariance flux underestimates over a grassland. *Agricultural and Forest Meteorology* 103, 279–300. doi:10.1016/S0168-1923(00)00123-4.